Journal of Computational Physics 229 (2010) 5518–5540

Contents lists available at ScienceDirect

Journal of Computational Physics

journal homepage: www.elsevier.com/locate/jcp

An Eulerian method for multi-component problems in non-linear elasticity with sliding interfaces

Philip T. Barton *, Dimitris Drikakis

Department of Aerospace Sciences, Cranfield University, Cranfield, Bedfordshire MK43 0AL, UK

ARTICLE INFO

Article history:
Received 13 July 2009
Received in revised form 16 February 2010
Accepted 6 April 2010
Available online 11 April 2010

Keywords:
Riemann problem
Level-set method
Ghost fluid method
Solid mechanics
Non-linear elasticity
WENO

ABSTRACT

This paper is devoted to developing a multi-material numerical scheme for non-linear elastic solids, with emphasis on the inclusion of interfacial boundary conditions. In particular for colliding solid objects it is desirable to allow large deformations and relative slide, whilst employing fixed grids and maintaining sharp interfaces. Existing schemes utilising interface tracking methods such as volume-of-fluid typically introduce erroneous transport of tangential momentum across material boundaries. Aside from combatting these difficulties one can also make improvements in a numerical scheme for multiple compressible solids by utilising governing models that facilitate application of high-order shock capturing methods developed for hydrodynamics. A numerical scheme that simultaneously allows for sliding boundaries and utilises such high-order shock capturing methods has not yet been demonstrated. A scheme is proposed here that directly addresses these challenges by extending a ghost cell method for gas-dynamics to solid mechanics, by using a first-order model for elastic materials in conservative form. Interface interactions are captured using the solution of a multi-material Riemann problem which is derived in detail. Several different boundary conditions are considered including solid/solid and solid/vacuum contact problems. Interfaces are tracked using level-set functions. The underlying single material numerical method includes a characteristic based Riemann solver and high-order WENO reconstruction. Numerical solutions of example multi-material problems are provided in comparison to exact solutions for the one-dimensional augmented system, and for a two-dimensional friction experiment.

1. Introduction

For modelling events such as high velocity impact and explosive loading of solid materials there is strong demand on the numerical methods to simultaneously achieve high wave resolution, maintain sharp interfaces, and accurately impose interfacial boundary conditions. Furthermore, given the probability of finite deformations it is desirable to employ fixed grids. In previous studies by the authors [2,3] a high-order shock capturing scheme was proposed for solid dynamics where Godunov's method was applied to an Eulerian model [7] in conservative form using fixed Cartesian grids. An important component of these is the solution of the Riemann problem at cell edges, which is used to evaluate the respective numerical flux functions. This is particularly advantageous from the viewpoint of resolving wave structures since material strength, an important source of non-linearity, is accounted for in the Riemann problem solution. Other similar models include [13,22,23], and numerical schemes include [14,18,28,30,31]. It is the purpose of this study to explore certain methods to be used in conjunction with these schemes to enable the solution of systems comprising multiple components.

* Corresponding author.
E-mail addresses: p.t.barton@cranfield.ac.uk (P.T. Barton), d.drikakis@cranfield.ac.uk (D. Drikakis).

0021-9991/$ - see front matter © 2010 Elsevier Inc. All rights reserved.
doi:10.1016/j.jcp.2010.04.012

The numerous numerical methods for solving multi-material problems using fixed grids can be broadly classed as either *interface capturing* or *interface tracking*. The former has been applied extensively to problems in fluid mechanics where the resultant interface smearing may be deemed acceptable on the basis that the flow is miscible. For many problems in solid mechanics however interfaces need to remain sharp and interface tracking methods are more suitable. Included in this category are level-set methods, volume-of-fluid (VOF) methods, and marker particle methods. A detailed presentation of the means by which an interface is evolved in each of these shall be omitted, and instead the interested reader is directed to the review in [24]. When interfaces of two solid materials come into contact two limits can be identified for the resulting behaviour: *stick* where both the traction and velocity vectors of each material normal to the common interface are equal; *slip* where tangential components of the traction normal to the interface are zero and the components slide freely over one another. In reality, for high velocity impacts the behaviour will lie somewhere in between these two limits [32], with the tangential motion a complex non-linear function of the interfacial state. An accurate numerical scheme for modelling such processes must incorporate an interface tracking method where the boundary evolution reflects the motion dictated by the physics. That is it allows unconstrained sliding between components. These requirements single out the level-set and marker particle methods. VOF methods on the other hand require a common velocity vector between interacting components within mixed cells. The next question then is how to incorporate these within a numerical scheme and more importantly how to account for the interaction between components.

The interest here is in an approach classed as a ghost fluid method (GFM), following the pioneering work in [5], as a means of treating interface interactions. The method assumes that one can identify using for example level-set functions those cells directly adjacent to and enclosing the interface. For each time iteration, the interface location is used to distinguish cells within each material's domain and those that are not, the latter are termed *ghost cells*. The ghost cells are then prescribed a state in such a way that when each material is advanced to the next time level using an independent single component solver the presence and resulting behaviour of material interfaces and their interactions are then captured. In [5] the ghost cell states are defined based upon the overlying state of the adjacent fluid and the boundary extrapolated entropy. In [15] it was proposed that solutions to the resulting multi-material Riemann problem at interfaces could be used to define the ghost cell states in what has become known as the modified ghost fluid method (MGFM). An immediate advantage of the ghost cell approach in general is that no additional terms enter into the governing physical equations and for the most part each material is treated independently. Furthermore the integral form of the governing equations need not be limited to the time dependent domain for each material; thus one need only consider flux functions for cell boundaries as per a single component solver. Ghost fluid type methods have been used in conjunction with an alternative formulation for solid materials in [29] for the study of impacting solids; in conjunction with a Lagrangian solid mechanics method in [6] to form a coupled solid/fluid scheme; and for solid/fluid problems in [17] utilising the compressible Euler equations with equations of state that enable simplified elastic–plastic response. Ghost fluid type methods have yet to be applied to any of the aforemention models for solid dynamics in conservative form.

The ghost fluid type methods are contrary to conservative methods such as in [19,9] where the integral form of the governing equations is solved for each material's (time dependent) region. The resulting finite volume numerical scheme thus requires reconstruction of the interface for calculation of cell apertures and volume fractions within mixed cells. Such methods have been successfully applied to the aforementioned models in conservative form, including in [19] where the VOF method is used in a coupled solid/fluid scheme, and in [30,31] where marker particles are used to track boundaries in the simulation of impacting solid materials. Although conservation is a desirable property it is recalled that only the level-set or marker particle method would accommodate the requirements for sliding material interfaces. Between these, extension of the level-set methods to multiple space dimensions is more straightforward, but are non-conservative by default. Using level-set functions to track interfaces in a conservative scheme such as in [9] could lead to difficulties in solid dynamics problems on account of mass loss. To exemplify this point consider a geometry with corners which would be typical to many problems in solid mechanics. Translating this through a grid using the level-set advection equation to evolve the boundaries will result in mass loss in the corner regions where characteristics converge and the inherent regularisation deletes the unresolved information (see [4]). Whilst modifications of the necessary numerical algorithms have been proposed that successfully suppress these errors, they are not entirely eliminated. Thus one can expect an error in the change in volume fraction in these regions across each time level. The result would be an erroneous computation of state variables potentially compromising numerical stability. From these considerations it is thus justified that if one is to employ level-set functions then a ghost fluid method should provide better stability.

The purpose of this paper is to extend the MGFM in [15] to the model of non-linear elasticity in conservative form from [7]. Thus far the MGFM has been applied only to problems on fixed grids where the materials are all fluid [15] or where materials that are considered solid are governed by the compressible hydrodynamics equations with an equation of state that allows simple elastoplastic response [17,34]. Application of the MGFM to models of solid mechanics in conservative form (which can be considered comprehensive in the sense that they can allow for multi-dimensional deformations) on fixed grids is yet to be achieved, and is justified on the basis of the following novel features:

- The ability to incorporate state-of-the-art shock capturing methods to a multi-material solid mechanics scheme: the use of models for solid materials in conservative form allows the retrofitting of established high-order numerical methods developed for hydrodynamic applications, which have proven to achieve superior wave resolution, to the field of solid dynamics. These capabilities are somewhat new even for single material problems.

- The sharp resolution of sliding interfaces on fixed grids: any artificial transport of tangential momentum between contacting surfaces, which previous schemes based upon the VOF method suffer, would be eliminated. Furthermore, the MGFM used in combination with level-set functions to track material boundaries allows a straightforward extension to multi-dimensions.
- The accurate imposition of interfacial boundary conditions: analysis of the MGFM for gas-dynamics in [16] showed that the imposition of boundary conditions is achieved to a higher degree of accuracy compared to the original GFM. Furthermore, in [15] it was demonstrated that although the GFM performs well for problems in fluid mechanics where waves impacting on an interface are of moderate strength, the method becomes inadequate for large sudden jumps in properties.

The rest of the paper proceeds as follows. In Section 2 the necessary theory is presented for non-linear elastic materials. The numerical scheme for the model is detailed in Section 3, along with a summary of the employed single component methods and boundary evolution equation. Section 4 is devoted to a detailed derivation of the Riemann problem solution for multi-materials, with focus on the characteristic relations and the applicable boundary conditions. The numerical scheme is demonstrated in Section 5 for selected initial value problems, for which exact solutions are available, using different interfacial boundary conditions and/or materials, and a two-dimensional friction experiment. Finally conclusions are drawn in Section 6.

2. Model of non-linear elasticity

The model for non-linear elastic materials can be written [7,25]

$$\frac{\partial \mathbf{U}}{\partial t}+\frac{\partial \mathcal{F}^k}{\partial x_k}=-\mathbf{S}^{\mathrm{C}}, \tag{1}$$

with

$$\mathbf{U}=\begin{pmatrix}\rho\mathbf{u}\\ \rho\mathbf{F}^{\mathrm{T}}\mathbf{e}_1\\ \rho\mathbf{F}^{\mathrm{T}}\mathbf{e}_2\\ \rho\mathbf{F}^{\mathrm{T}}\mathbf{e}_3\\ \rho E\end{pmatrix},\quad \mathcal{F}^k=\begin{pmatrix}u_k\rho\mathbf{u}-\sigma\mathbf{e}_k\\ u_k\rho\mathbf{F}^{\mathrm{T}}\mathbf{e}_1-u_1\rho\mathbf{F}^{\mathrm{T}}\mathbf{e}_k\\ u_k\rho\mathbf{F}^{\mathrm{T}}\mathbf{e}_2-u_2\rho\mathbf{F}^{\mathrm{T}}\mathbf{e}_k\\ u_k\rho\mathbf{F}^{\mathrm{T}}\mathbf{e}_3-u_3\rho\mathbf{F}^{\mathrm{T}}\mathbf{e}_k\\ u_k\rho E-(\sigma\mathbf{u})\mathbf{e}_k\end{pmatrix},\quad \mathbf{S}^{\mathrm{C}}=\begin{pmatrix}0\\ u_1\nabla\cdot(\rho\mathbf{F})\\ u_2\nabla\cdot(\rho\mathbf{F})\\ u_3\nabla\cdot(\rho\mathbf{F})\\ 0\end{pmatrix},$$

where $\mathbf{u}=[u_i]$ is the velocity vector; $\mathbf{F}=[F_{ij}]$ is the tensor of deformation gradients; $\sigma=[\sigma_{ij}]$ is the symmetric Cauchy stress tensor; $\rho=\rho_0/\det|\mathbf{F}|$ is the density, with ρ_0 a constant reference density in the unstressed state; $E=(\mathcal{E}+|\mathbf{u}|^2/2)$ is the total energy; and $\mathbf{e}_k$ are the Cartesian unit vectors. Summation is assumed over repeated indices. The specific internal energy $\mathcal{E}$ is found from a hyperelastic equation of state in terms of the principal invariants $\mathcal{I}_1=\mathrm{tr}(\mathbf{G})$, $\mathcal{I}_2=\frac{1}{2}[(\mathrm{tr}(\mathbf{G}))^2-\mathrm{tr}(\mathbf{G}^2)]$, $\mathcal{I}_3=\det|\mathbf{G}|$, of the Finger strain tensor $\mathbf{G}=\mathbf{F}^{-\mathrm{T}}\mathbf{F}^{-1}$; and entropy S:

$$\mathcal{E}(\mathcal{I}_1,\mathcal{I}_2,\mathcal{I}_3,S)=\frac{K_0}{2\alpha^2}(\mathcal{I}_3^{\alpha/2}-1)^2+c_vT_0\mathcal{I}_3^{\gamma/2}(\exp[S/c_v]-1)+\frac{B_0}{2}\mathcal{I}_3^{\beta/2}(\mathcal{I}_1^2/3-\mathcal{I}_2), \tag{2}$$

where $K_0=c_0^2-(4/3)b_0^2$, $B_0=b_0^2$ are the squared bulk speed of sound and the squared speed of the shear wave respectively; c_v is the heat capacity at constant volume; and α,β,γ are constants characterising the non-linear dependence of sound speeds and temperature on the density. The stress tensor is found from

$$\sigma_{ij}=\rho F_{ik}\frac{\partial\mathcal{E}}{\partial F_{jk}}. \tag{3}$$

The terms on the right-hand-side of the equations for $\mathbf{F}$ in Eq. (1) stem from the three compatibility constraints

$$\nabla\cdot(\rho\mathbf{F})=0. \tag{4}$$

In fact Eq. (4) is deduced from six compatibility conditions for the inverse deformation gradient $\mathbf{g}=\mathbf{F}^{-1}$ [2,7], since $\mathbf{g}$ can be used to derive an alternative formulation governing the conservation of strain [7,22]. It is necessary that Eq. (4) be satisfied for all time. It is mentioned that this is not necessarily true of numerical computations of the multi-dimensional system Eq. (1) with $\mathbf{S}^{\mathrm{C}}=0$ as a result of truncation errors [18] and instead the terms in $\mathbf{S}^{\mathrm{C}}$ are treated as source terms in the numerical computation. For the augmented one-dimensional system, upon which much of this study is focused, Eq. (4) will hold for all time if satisfied initially. Thus for the one-dimensional case $\mathbf{S}^{\mathrm{C}}$ can be ignored in the discretisation of Eq. (1).

Knowledge of the eigenvalues and eigenvectors of the system Eq. (1) reduced to quasi-linear form is essential for the method used within the numerical scheme to compute the flux functions. A detailed derivation of the decomposition to canonical form has been presented elsewhere [2,3] and thus, for clarity, details are left to the appendix.

3. Modified ghost fluid method

3.1. Material interaction

Although the numerical methods employed for multiple interacting materials are applicable to any of the interface tracking techniques, for the reasons mentioned in Section 1, level-set functions are used. For a system comprising multiple materials, each component, denoted by α, is assumed to occupy the region $\Gamma^\alpha(t)$. In the course of the computation each region is identifiable by defining a level-set function, $\phi^\alpha(\mathbf{x},t)$, that at every point in space and time represents the signed Euclidean distance from the interface. Thus the zero isocontour of ϕ^α marks the location of a material interface, $\partial\Gamma^\alpha(t) = \{\mathbf{x}:\phi^\alpha(x) = 0\}$, while a positive value distinguishes those regions occupied by the corresponding medium, and a negative value those that are not. For each material then:

$$\phi^\alpha(\mathbf{x},t)\begin{cases} > 0, & \mathbf{x} \in \Gamma^\alpha(t) \\ = 0, & \mathbf{x} \in \partial\Gamma^\alpha(t) \\ < 0, & \mathbf{x} \notin \Gamma^\alpha(t) \end{cases}.$$

In fact, one need only employ $N-1$ level-set functions for a system of N materials.

For clarity the details of the modified ghost fluid method for interface interactions shall be presented initially for the special case of one spatial dimension. It is assumed a computational mesh is employed where cell centred quantities are denoted by the indices i and cell boundaries by $i \pm 1/2$; thus each cell is denoted $I_i = [x_{i-1/2}, x_{i+1/2}]$ and has the size $(\Delta x)_i = x_{i+1/2} - x_{i-1/2}$. Space averages of the state variables, and values of the level-set functions at the current time level t^n, are stored at cell centres. For an interface located between grid points i and $i+1$ (Fig. 1(a)), identifiable by $\phi_i \cdot \phi_{i+1} > 0$, the material to the left of the interface has the set of ghost cells $\{I_{i+1}, I_{i+2}, \ldots, I_{i+N_f+1}\}$ where N_f denotes the number of fictitious points required by the numerical stencil for the employed single component solver. The known states $\mathbf{U}^{\mathrm{L}} = \mathbf{U}(x_i, t^n)$ and $\mathbf{U}^{\mathrm{R}} = \mathbf{U}(x_{i+1}, t^n)$ at the current time level for the left and right materials respectively can be used to pose a multi-material Riemann problem across the interface with the initial condition:

$$\mathbf{U}(t=0,x) = \begin{cases} \mathbf{U}^{\mathrm{L}} & \text{if} \quad x \leqslant x_0, \\ \mathbf{U}^{\mathrm{R}} & \text{if} \quad x > x_0. \end{cases} \tag{5}$$

with x_0 an arbitrary point in space. The solutions $\widetilde{\mathbf{U}}^{\mathrm{L/R}}$, found using the procedure to be explained in detail in Section 4, are used to define the state of the respective material's ghost cell immediately adjacent to the boundary (e.g. cell I_{i+1} for the left hand material in Fig. 1). In fact all other ghost cells are also taken to have the extrapolated predicted state. Thus, in general, within every cell of the computational mesh the state of the real material at that point is stored along with the ghost state of the neighbouring material.

An anomaly observed in gas-dynamics that can degrade the resolution of problems with interfaces is the so called 'heating' errors. These errors appear as deviations from the true solution in certain state variables, such as density and entropy, in the vicinity of the interface. In [5] a simple and effective fix was proposed for this problem in conjunction with the original ghost fluid method: for a material to the left of an interface located between cells I_i and I_{i+1}, the real cell I_i immediately adjacent to the boundary takes the value of entropy from the cell I_{i-1}. The fix applied to the right material follows by symmetry. With the fix carried out prior to the interface interaction computation the value of entropy from cell I_{i-1} is also prescribed to the ghost cells since $\partial S = 0$ at the boundary. This concept is illustrated in Fig. 1(b). In the examples to follow the extent to which the entropy fix suppresses heating errors shall be investigated for problems in solid mechanics.

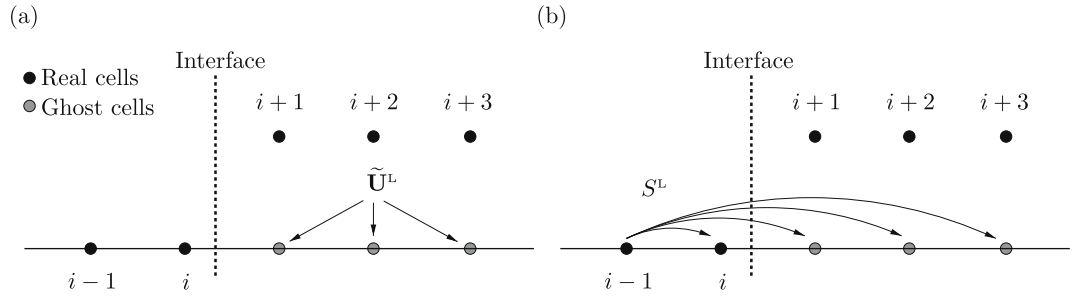

Fig. 1. Illustration of the modified ghost fluid method; (a) the prescription of ghost cell states for a material to the left of the interface using the solution $\widetilde{\mathbf{U}}^{\mathrm{L}}$ of the multimaterial Riemann problem; (b) the entropy fix.

3.2. Numerical scheme for single components

Having defined the ghost cell states the governing equations for each material are solved independently for the next time level. For each material a solution is sought only for real cells and the ghost cells immediately adjacent to boundaries. In two space dimensions the governing transport equations Eq. (1) are solved using a fixed, structured computational grid consisting of quadrilateral cells, denoted $I_{i,j}$, using the method presented in [3], where the indices i,j are used to denote cell centred quantities. Each cell $I_{i,j}$ has the dimensions $\Delta x_{1_{i,j}} = x_{1_{i+1/2,j}} - x_{1_{i-1/2,j}}$, $\Delta x_{2_{i,j}} = x_{2_{i,j+1/2}} - x_{2_{i,j-1/2}}$. Using the method-of-lines approach the discretised system for each material reads:

$$\frac{\mathrm{d}}{\mathrm{d}t}\mathbf{U}^{\alpha}_{i,j}(t) = -\left\{\frac{\mathcal{F}^{1}_{i+1/2,j} - \mathcal{F}^{1}_{i-1/2,j,k}}{\Delta x_{1_{i,j}}} + \frac{\mathcal{F}^{2}_{i,j+1/2} - \mathcal{F}^{2}_{i,j-1/2}}{\Delta x_{2_{i,j}}}\right\}. \tag{6}$$

where $\mathbf{U}^{\alpha}_{i,j}$ and $\mathcal{F}^{k,\alpha}$ are the cell averaged state and intercell numerical flux functions respectively for material α. To solve the multi-dimensional problem Eq. (6) an unsplit dimension-by-dimension approach is used. For this, each numerical flux function is calculated via solution of a one-dimensional Riemann problem orientated normal to the respective boundary. Evaluation of the right-hand-side (RHS) of Eq. (6) therefore involves computing the solutions of four one-dimensional Riemann problems: one across each cell boundary for each cell in the two-dimensional calculation. Only once all the numerical fluxes are summed according to the RHS of Eq. (6) is the solution advanced in time. The temporal derivatives in Eq. (6) are integrated using the 3rd-order TVD Runge–Kutta (RK) method from [26]. At the start of every time level, the timestep is calculated from

$$\Delta t = C \times \min_{i,j}\left(\frac{\Delta x_1}{\max\limits_{\alpha}(\lambda_1)}, \frac{\Delta x_2}{\max\limits_{\alpha}(\lambda_2)}\right),$$

where $\max_{\alpha}(\lambda_{\eta})$ is the maximum wavespeed in the direction η for each material α, and $0 < C \leqslant 1$ is an adjustable scaler parameter used to control the timestep so as to satisfy the Courant–Friedrichs–Lewy condition. It remains only to specify the method used for computing the numerical flux functions.

Across each cell boundary the numerical flux functions are computed using approximate solutions to the local Riemann problem found using the high-order characteristics based method presented in [2]. Briefly this method comprises computing exact solutions of the system Eq. (1) reduced to quasi-linear form with linearised Jacobian. Considering for example the x_1-direction, the linearised Jacobian is evaluated at the intercell state $\widehat{\mathbf{W}}_{i\pm1/2}$, where $\mathbf{W}$ is the vector of primitive variables [cf. Eq. (A.2)], taken to be a simple arithmetic mean of the adjoining left and right cell centre states: $\widehat{\mathbf{W}}_{i\pm1/2} = \frac{1}{2}(\mathbf{W}_i + \mathbf{W}_{i\pm1})$.

It is mentioned that, whilst the characteristic based approach for solving the local Riemann problems has been shown to exhibit very good wave capturing capabilities and is adequate for the examples presented in this paper, linearised Riemann solvers for non-linear elasticity are known to suffer some deficiencies. In [28], where the performance of a number of different approximate Riemann solvers for the equations of non-linear elasticity was examined, the linearised solver was shown to fail in the face of strong impacts, and produced entropy violating shock waves in cases of sonic rarefactions (although it is pointed out that this latter condition is rare in solid media).

High-order spatial accuracy is achieved by reconstructing the cell averaged states projected onto the characteristic space using the 5th-order weighted essentially non-oscillatory (WENO-5) method from [10] with monotonicity preserving constraints of [1] to provide the initial left and right states, $\mathbf{U}^{\mathrm{L}}/\mathrm{R}$. Although it is expected that the use of the fifth-order reconstruction scheme will act to reduce ultimately observed errors in the solution, the actual order of accuracy of the scheme is restricted to 3rd-order by the choice of temporal integration method. Evaluation of the benefits of using higher-order spatial reconstruction, in terms of overall accuracy, will thus form part of the analysis in the examples section.

3.3. Interface evolution

The interface evolves according to the level-set convection equation

$$\frac{\partial \phi^{\alpha}}{\partial t} + u_{\eta}\frac{\partial \phi^{\alpha}}{\partial x_{\eta}} = 0. \tag{7}$$

As with the governing transport equations for the solid components, Eq. (7) is also solved using the method-of-lines; spatial derivatives are discretised using the 5th-order central scheme presented in [21] and time integration is performed using the same 3rd-order RK method as for the material equations.

In the computations of the boundary evolution equations the temporal updates using the RK method are performed harmoniously with the material equations for each sub-stage. The reason being the interface interaction calculation is carried out for each sub-stage for those cells that enclose the interface and from which the time-local interface velocity can be used in Eq. (7) for a more accurate overall boundary advection. Away from the interface, where velocities for the corresponding iso-contours are unknown, the interface velocity can be extrapolated to all cells using Eq. (9).

It is mentioned that level-set methods are by default non-conservative and spurious conservation errors can occur, in particular for multi-dimensional problems. For problems in solid mechanics, these errors can be expected to appear where the

described geometry develops thin ligaments or has corners where characteristics converge (see for example [4] and the particle level-set method proposed therein as a means of reducing these errors). In the examples considered here, mass conservation errors are suppressed using the above described high-order spatial discretisation methods in the evaluation of Eq. (7).

Another cause is that for multi-dimensional problems the boundary extrapolated velocity does not necessarily correspond exactly to the velocities for each isocontour paramount to ensuring that ϕ remains a signed-distance function, i.e. the velocities which when used in Eq. (7) ensure that the updated level-set function at each point satisfies the Eikonal equation $|\nabla\phi| = 1$. Reinitialisation algorithms (see for example [27,8]) are thus required incrementally to reinstate this property. Reinitialisation of the level-set fields can be achieved by solving to steady state the following PDE:

$$\frac{\partial\phi}{\partial\tau} + S(\phi)(|\nabla\phi| - 1) = \mathcal{F}(\phi), \tag{8}$$

where τ is fictitious time and $S(\phi)$, $\mathcal{F}(\phi)$ are functions to be determined. In the original method of Sussman et al. [27] $\mathcal{F} = 0$ and $S(\phi) = \text{sign}(\phi)$ in Eq. (8), however it is well known that this leads to spurious movement of the zero level-set isocontour, and proves to be particularly problematic in the vicinity of corners. To avoid these artifacts, the recent method proposed by Hartman et al. [8] is used where $S(\phi) = \text{sign}(\phi)$ as in the original method, but $\mathcal{F}$ is formulated in such a way that the zero-level isocontour remains anchored to the position prior to the advent of reinitialisation. Details of the function $\mathcal{F}(\phi)$ are quite lengthy and are thus not repeated here. Spatial derivatives in Eq. (8) are computed using the 5th-order WENO method presented in [11]. It is found that this method remains robust in the face of level-set fields of large curvatures and successfully anchors the zero level-set to the original position.

3.4. Multi-dimensional implementation

The order of proceedings for the MGFM implemented in multi-dimensions does not depart from the one-dimensional case, rather certain components of the method become slightly more involved. In the first instance, boundary cells can be identified by checking for sign changes in the level-set functions as with the one-dimensional approach, only now this check is performed in each coordinate direction. The main difficulty one faces in implementing the MGFM in multi-dimensions is how to define the left and right states for the Riemann problem initial conditions Eq. (5). Whereas in one-dimension the interface lies normal to the Cartesian axis along which the solution is sought, and intersects some point between two adjacent cell centres, in multi-dimensions it is quite likely that the interface may lie at some arbitrary angle to these axis. Consider the case where a ghost cell state is sought for Solid 1 that is in contact with Solid 2. Ideally, when solving the Riemann problem in a given ghost cell immediately adjacent to the boundary (from hereon named *boundary ghost cells*) for Solid 1, one would like to have knowledge of the state extrapolated in a sensible way from the neighbouring real cells (from hereon named *boundary real cells*). In order to facilitate this approach, any state quantity q of Solid 1 can be extrapolated from the boundary real cells along the interface normal trajectory by solving to steady state the following PDE [5]:

$$\frac{\partial q}{\partial\tau} \pm n_k \frac{\partial q}{\partial x_k} = 0, \tag{9}$$

where τ is fictitious time, the ± operator is used to define the direction of extrapolation, and $\mathbf{n}$ is the unit normal to the level-set isocontour:

$$\mathbf{n} = \frac{\nabla\phi}{|\nabla\phi|}. \tag{10}$$

Thus, within the boundary ghost cells of Solid 1, one can obtain the extrapolated state of Solid 1, $\mathbf{U}^{S1,EXT}$, and has the underlying real state of Solid 2, $\mathbf{U}^{S2}$. To account for the arbitrary angle of the interface with respect to the Cartesian axis, the state variables for both materials within the boundary ghost cells must be rotated onto the coordinate system defined by the interface normal. This can be easily achieved by using the local interface normal computed from the level-set field (using Eq. (10)) to define a rotation matrix $\mathbf{R}^{ROT} = \mathbf{R}^{ROT}(\mathbf{n})$ (see [19]) and subsequently rotating the velocity and deformation tensor as follows:

$$\begin{pmatrix} \mathbf{u} \\ \mathbf{F} \\ S \end{pmatrix}^{ROT} = \begin{pmatrix} \mathbf{R}^{ROT}\mathbf{u} \\ \mathbf{R}^{ROT}\mathbf{F}\mathbf{R}^{ROT^T} \\ S \end{pmatrix}. \tag{11}$$

The initial conditions for the Riemann problem thus become: $\mathbf{U}^L = (\mathbf{U}^{S1,EXT})^{ROT}$ and $\mathbf{U}^R = (\mathbf{U}^{S2})^{ROT}$. The subsequent components of the method then follow the one-dimensional procedure. Once the solution has been computed one need only rotate the resultant state back to the Cartesian coordinate system using the inverse of Eq. (11).

The implementation of the MGFM in multi-dimensions can be summarised as follows:

Step 1: Using the level-set field(s) at the current time level, all real cells and those cells that can be classified as ghost cells, based upon the previously described criteria, are distinguished for computation.

Step 2: For each material, the state of boundary real cells is extrapolated along the interface normal trajectory to all boundary ghost cells. Also, if the entropy fix is being used this can be incorporated into the same extrapolation routine at this stage.

Step 3: A multi-material Riemann problem is solved within all boundary ghost cells using the extrapolated states and, for the case of solid/solid contact problems, the underlying real state of the adjacent material, rotated normal to the interface. The solution (rotated back to the Cartesian coordinate system) is subsequently extrapolated to all other ghost cells.

Step 4: One is then free to use the chosen numerical scheme for single component problems to update each material independently to the next time level. In general this involves solving for each cell within the computational domain regardless of whether it is a real cell or a ghost cell. In practice however one need only solve for those real cells and a narrow band of boundary ghost cells surrounding the material.

Step 5: The level-set field(s) are then updated to the next time level using as the velocity vector at each point the extrapolated interface velocities determined from solution of the boundary Riemann problems. After the updated level-set field (s) have been obtained, each is reinitialised to ensure compliance with the Eikonal condition.

Steps 1–5 are repeated for each time level in the computation.

4. Multi-material Riemann problems

The multi-material Riemann problem details depend on the materials on either side of the interface, which could be solid or vacuum, and the orientation with respect to the interface of the material for which the solution is sought. Sample solutions are depicted in Fig. 2. In what follows the multi-material Riemann problem is considered in one-dimension to be specified. Where appropriate, any corresponding state quantity shall be identifiable by superscript L or R, for left and right materials respectively, assuming that these states are rotated normal to the interface (as per the previous section). Emphasis shall be placed on the solution for the left hand material, but it is found that the solution for the converse differs only by sign on certain terms and these shall be identified clearly.

For each solid material, the following thirteen invariant relations can be written:

$$\mathbf{\Phi}^{\mathrm{L/R}} \equiv \mathbf{L}^{\mathrm{L/R}} \cdot \partial \mathbf{W}^{\mathrm{L/R}} = 0. \tag{12}$$

Recall that the rows of $\mathbf{L}^{\mathrm{L/R}}$ are the left eigenvectors of the linearised Jacobian matrix Eq. (A.3) and correspond to the wavespeeds with canonical ordering in Eq. (A.5). For the left material of the multi-material Riemann problem one can utilise the invariants corresponding to the three non-linear waves with speeds $u_1\mathbf{I} + \mathcal{D}$ and contact: $\Phi_j, 4 \leqslant j \leqslant 13$. Partial derivatives in each of these relations can be replaced with differences according to

$$\partial \mathbf{W}^{\mathrm{L/R}} \approx \Delta \mathbf{W}^{\mathrm{L/R}} \equiv \widetilde{\mathbf{W}}^{\mathrm{L/R}} - \mathbf{W}^{\mathrm{L/R}}, \tag{13}$$

where $\widetilde{\mathbf{W}}^{\mathrm{L/R}}$ denotes the primitive state of the left hand material at the interface, and $\mathbf{W}^{\mathrm{L/R}}$ is the state at the current time level just inside the boundary, which for an interface located between cells I_i and I_{i+1} can be taken to be $\mathbf{W}^{\mathrm{L}} = \mathbf{W}(\mathbf{U}_i)$ and $\mathbf{W}^{\mathrm{R}} = \mathbf{W}(\mathbf{U}_{i+1})$. The linearised coefficients are also taken to be evaluated from these states for each respective material. Thus, for each solid at the boundary one has ten relations for the thirteen unknowns; consideration of the boundary conditions is required to yield the additional relations.

It is usual in solid mechanics problems to prescribe the interfacial boundary conditions in terms of restrictions on the interface velocities $\widetilde{\mathbf{u}}$, and/or the traction $\tilde{\sigma}\mathbf{e}_n$, where $\mathbf{e}_n$ is the normal to the interface. Note that $\mathbf{e}_n = \mathbf{e}_\eta$ for the one-dimensional case in the η-direction, and more specifically for variables rotated using Eq. (11) (such that they are rotated onto the

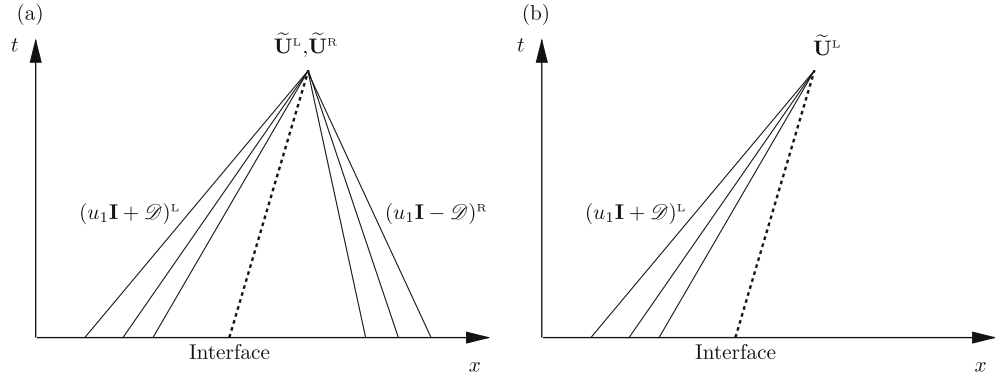

Fig. 2. *x–t* plots of example multi-material Riemann problem solutions for: (a) solid on left in contact with another solid on right and (b) solid on left in contact with a vacuum.

x_1-direction) $\eta = 1$ can be taken. It will be seen that the number of boundary conditions must necessarily coincide with the number of non-linear waves. From Eq. (3) and since $\mathcal{E} = \mathcal{E}(\mathbf{F}, S)$ stress is a function of $\mathbf{F}$ and S. The traction at the boundary can be approximated by a power series around the state $(\mathbf{F}^{L/R}, S^{L/R})$ inside the boundary:

$$\sigma_{\eta i}(\widetilde{\mathbf{F}}^{L/R}, \widetilde{S}^{L/R}) = \sigma_{\eta i}(\mathbf{F}^{L/R}, S^{L/R}) + \frac{\partial \sigma_{\eta i}}{\partial F_{jk}}(\mathbf{F}^{L/R}, S^{L/R})\left[\widetilde{F}_{jk}^{L/R} - F_{jk}^{L/R}\right] + \frac{\partial \sigma_{\eta i}}{\partial S}(\mathbf{F}^{L/R}, S^{L/R})\left[\widetilde{S}^{L/R} - S^{L/R}\right] + \cdots \tag{14}$$

Neglecting higher-order terms and using the definitions of the coefficients in Eqs. (A.4) and (14) can be rewritten as

$$\tilde{\sigma}_{\eta i}^{L/R} = \sigma_{\eta i}^{L/R} + \rho^{L/R}\left[A_{ik}^{\eta 1}\left(\widetilde{\mathbf{F}} - \mathbf{F}\right)_{1k} + A_{ik}^{\eta 2}\left(\widetilde{\mathbf{F}} - \mathbf{F}\right)_{2k} + A_{ik}^{\eta 3}\left(\widetilde{\mathbf{F}} - \mathbf{F}\right)_{3k} + B_i^{\eta}\left(\widetilde{S} - S\right)\right]^{L/R}. \tag{15}$$

Thus combining Eq. (15) with the applicable invariants gives thirteen equations for sixteen unknowns:

$$\widehat{\mathbf{L}}^{L/R}\left[\begin{pmatrix} \tilde{\mathbf{u}} \\ \widetilde{\mathbf{F}}^{T}\mathbf{e}_1 \\ \widetilde{\mathbf{F}}^{T}\mathbf{e}_2 \\ \widetilde{\mathbf{F}}^{T}\mathbf{e}_3 \\ \widetilde{S} \end{pmatrix}^{L/R} - \begin{pmatrix} \mathbf{u} \\ \mathbf{F}^{T}\mathbf{e}_1 \\ \mathbf{F}^{T}\mathbf{e}_2 \\ \mathbf{F}^{T}\mathbf{e}_3 \\ S \end{pmatrix}^{L/R}\right] - \frac{1}{\rho^{L/R}}\begin{pmatrix} 0 \\ 0 \\ 0 \\ 0 \\ (\tilde{\sigma}^{L/R} - \sigma^{L/R})\mathbf{e}_\eta \end{pmatrix} = 0, \tag{16}$$

where

$$\widehat{\mathbf{L}} = \left(\hat{\mathbf{l}}_1, \hat{\mathbf{l}}_2, \hat{\mathbf{l}}_3, \hat{\mathbf{l}}_4, \hat{\mathbf{l}}_5, \hat{\mathbf{l}}_6, \hat{\mathbf{l}}_7, \hat{\mathbf{l}}_8, \hat{\mathbf{l}}_9, \hat{\mathbf{l}}_{10}, \hat{\mathbf{l}}_{11}, \hat{\mathbf{l}}_{12}, \hat{\mathbf{l}}_{13}\right)^{T}, \tag{17}$$

with

$$\hat{\mathbf{l}}_1 = \left((\mathcal{D}\mathbf{Q})_{11}, (\mathcal{D}\mathbf{Q})_{12}, (\mathcal{D}\mathbf{Q})_{13}, \xi Q_{1i}A_{i1}^{\eta 1}, \xi Q_{1i}A_{i2}^{\eta 1}, \xi Q_{1i}A_{i3}^{\eta 1}, \xi Q_{1i}A_{i1}^{\eta 2}, \xi Q_{1i}A_{i2}^{\eta 2}, \xi Q_{1i}A_{i3}^{\eta 2}, \xi Q_{1i}A_{i1}^{\eta 3}, \xi Q_{1i}A_{i2}^{\eta 3}, \xi Q_{1i}A_{i3}^{\eta 3}, \xi Q_{1i}B_i^{\eta}\right),$$

$$\hat{\mathbf{l}}_2 = \left((\mathcal{D}\mathbf{Q})_{21}, (\mathcal{D}\mathbf{Q})_{22}, (\mathcal{D}\mathbf{Q})_{23}, \xi Q_{2i}A_{i1}^{\eta 1}, \xi Q_{2i}A_{i2}^{\eta 1}, \xi Q_{2i}A_{i3}^{\eta 1}, \xi Q_{2i}A_{i1}^{\eta 2}, \xi Q_{2i}A_{i2}^{\eta 2}, \xi Q_{2i}A_{i3}^{\eta 2}, \xi Q_{2i}A_{i1}^{\eta 3}, \xi Q_{2i}A_{i2}^{\eta 3}, \xi Q_{2i}A_{i3}^{\eta 3}, \xi Q_{2i}B_i^{\eta}\right),$$

$$\hat{\mathbf{l}}_3 = \left((\mathcal{D}\mathbf{Q})_{31}, (\mathcal{D}\mathbf{Q})_{32}, (\mathcal{D}\mathbf{Q})_{33}, \xi Q_{3i}A_{i1}^{\eta 1}, \xi Q_{3i}A_{i2}^{\eta 1}, \xi Q_{3i}A_{i3}^{\eta 1}, \xi Q_{3i}A_{i1}^{\eta 2}, \xi Q_{3i}A_{i2}^{\eta 2}, \xi Q_{3i}A_{i3}^{\eta 2}, \xi Q_{3i}A_{i1}^{\eta 3}, \xi Q_{3i}A_{i2}^{\eta 3}, \xi Q_{3i}A_{i3}^{\eta 3}, \xi Q_{3i}B_i^{\eta}\right),$$

$$\hat{\mathbf{l}}_4 = \mathbf{l}_4, \qquad \hat{\mathbf{l}}_5 = \mathbf{l}_5, \qquad \hat{\mathbf{l}}_6 = \mathbf{l}_6, \qquad \hat{\mathbf{l}}_7 = \mathbf{l}_7,$$

$$\hat{\mathbf{l}}_8 = \mathbf{l}_8, \qquad \hat{\mathbf{l}}_9 = \mathbf{l}_9, \qquad \hat{\mathbf{l}}_{10} = \mathbf{l}_{10},$$

$$\hat{\mathbf{l}}_{11} = (0, 0, 0, A_{11}^{\eta 1}, A_{12}^{\eta 1}, A_{13}^{\eta 1}, A_{11}^{\eta 2}, A_{12}^{\eta 2}, A_{13}^{\eta 2}, A_{11}^{\eta 3}, A_{12}^{\eta 3}, A_{13}^{\eta 3}, B_1^{\eta}),$$

$$\hat{\mathbf{l}}_{12} = (0, 0, 0, A_{21}^{\eta 1}, A_{22}^{\eta 1}, A_{23}^{\eta 1}, A_{21}^{\eta 2}, A_{22}^{\eta 2}, A_{23}^{\eta 2}, A_{21}^{\eta 3}, A_{22}^{\eta 3}, A_{23}^{\eta 3}, B_2^{\eta}),$$

$$\hat{\mathbf{l}}_{13} = (0, 0, 0, A_{31}^{\eta 1}, A_{32}^{\eta 1}, A_{i3}^{\eta 1}, A_{31}^{\eta 2}, A_{32}^{\eta 2}, A_{33}^{\eta 2}, A_{31}^{\eta 3}, A_{32}^{\eta 3}, A_{33}^{\eta 3}, B_3^{\eta}).$$

The parameter $\xi = \pm 1$ has been included in Eq. (17) to distinguish the direction of the non-linear waves: $\xi = +1$ if the material is on the left, $\xi = -1$ if on the right. The inverse of Eq. (17) is

$$\widehat{\mathbf{R}} = (\hat{\mathbf{r}}_1, \hat{\mathbf{r}}_2, \hat{\mathbf{r}}_3, \hat{\mathbf{r}}_4, \hat{\mathbf{r}}_5, \hat{\mathbf{r}}_6, \hat{\mathbf{r}}_7, \hat{\mathbf{r}}_8, \hat{\mathbf{r}}_9, \hat{\mathbf{r}}_{10}, \hat{\mathbf{r}}_{11}, \hat{\mathbf{r}}_{12}, \hat{\mathbf{r}}_{13}), \tag{18}$$

where

$$\hat{\mathbf{r}}_1 = ((\mathcal{D}\mathbf{Q})_{11}^{-1}, (\mathcal{D}\mathbf{Q})_{21}^{-1}, (\mathcal{D}\mathbf{Q})_{31}^{-1}, 0, 0, 0, 0, 0, 0, 0, 0, 0, 0)^{T},$$

$$\hat{\mathbf{r}}_2 = ((\mathcal{D}\mathbf{Q})_{12}^{-1}, (\mathcal{D}\mathbf{Q})_{22}^{-1}, (\mathcal{D}\mathbf{Q})_{32}^{-1}, 0, 0, 0, 0, 0, 0, 0, 0, 0, 0)^{T},$$

$$\hat{\mathbf{r}}_3 = ((\mathcal{D}\mathbf{Q})_{13}^{-1}, (\mathcal{D}\mathbf{Q})_{23}^{-1}, (\mathcal{D}\mathbf{Q})_{33}^{-1}, 0, 0, 0, 0, 0, 0, 0, 0, 0, 0)^{T},$$

$$\hat{\mathbf{r}}_4 = \mathbf{r}_4, \quad \hat{\mathbf{r}}_5 = \mathbf{r}_5, \quad \hat{\mathbf{r}}_6 = \mathbf{r}_6, \quad \hat{\mathbf{r}}_7 = \mathbf{r}_7,$$

$$\hat{\mathbf{r}}_8 = \mathbf{r}_8, \quad \hat{\mathbf{r}}_9 = \mathbf{r}_9, \quad \hat{\mathbf{r}}_{10} = \mathbf{r}_{10},$$

$$\hat{\mathbf{r}}_{11} = \left(\xi(\mathbf{Q}^{-1}\mathcal{D}\mathbf{Q})^{-1}_{11}, \xi(\mathbf{Q}^{-1}\mathcal{D}\mathbf{Q})^{-1}_{21}, \xi(\mathbf{Q}^{-1}\mathcal{D}\mathbf{Q})^{-1}_{31}, F_{\eta 1}\Omega^{-1}_{11}, F_{\eta 2}\Omega^{-1}_{11}, F_{\eta 3}\Omega^{-1}_{11}, F_{\eta 1}\Omega^{-1}_{21}, F_{\eta 2}\Omega^{-1}_{21}, F_{\eta 3}\Omega^{-1}_{21}, F_{\eta 1}\Omega^{-1}_{31}, F_{\eta 2}\Omega^{-1}_{31}, F_{\eta 3}\Omega^{-1}_{31}, 0\right)^{\mathrm{T}},$$

$$\hat{\mathbf{r}}_{12} = \left(\xi(\mathbf{Q}^{-1}\mathcal{D}\mathbf{Q})^{-1}_{12}, \xi(\mathbf{Q}^{-1}\mathcal{D}\mathbf{Q})^{-1}_{22}, \xi(\mathbf{Q}^{-1}\mathcal{D}\mathbf{Q})^{-1}_{32}, F_{\eta 1}\Omega^{-1}_{12}, F_{\eta 2}\Omega^{-1}_{12}, F_{\eta 3}\Omega^{-1}_{12}, F_{\eta 1}\Omega^{-1}_{22}, F_{\eta 2}\Omega^{-1}_{22}, F_{\eta 3}\Omega^{-1}_{22}, F_{\eta 1}\Omega^{-1}_{32}, F_{\eta 2}\Omega^{-1}_{32}, F_{\eta 3}\Omega^{-1}_{32}, 0\right)^{\mathrm{T}},$$

$$\hat{\mathbf{r}}_{13} = \left(\xi(\mathbf{Q}^{-1}\mathcal{D}\mathbf{Q})^{-1}_{13}, \xi(\mathbf{Q}^{-1}\mathcal{D}\mathbf{Q})^{-1}_{23}, \xi(\mathbf{Q}^{-1}\mathcal{D}\mathbf{Q})^{-1}_{33}, F_{\eta 1}\Omega^{-1}_{13}, F_{\eta 2}\Omega^{-1}_{13}, F_{\eta 3}\Omega^{-1}_{13}, F_{\eta 1}\Omega^{-1}_{23}, F_{\eta 2}\Omega^{-1}_{23}, F_{\eta 3}\Omega^{-1}_{23}, F_{\eta 1}\Omega^{-1}_{33}, F_{\eta 2}\Omega^{-1}_{33}, F_{\eta 3}\Omega^{-1}_{33}, 0\right)^{\mathrm{T}}.$$

Thus Eq. (16) can be rewritten

$$\widetilde{\mathbf{W}}^{\mathrm{L/R}} = \mathbf{W}^{\mathrm{L/R}} + \frac{1}{\rho^{\mathrm{L/R}}}\left[\hat{\mathbf{r}}_{11}(\tilde{\sigma}_{\eta 1} - \sigma_{\eta 1}) + \hat{\mathbf{r}}_{12}(\tilde{\sigma}_{\eta 2} - \sigma_{\eta 2}) + \hat{\mathbf{r}}_{13}(\tilde{\sigma}_{\eta 3} - \sigma_{\eta 3})\right]^{\mathrm{L/R}}. \tag{19}$$

It remains then to specify values of the traction at the boundary $\tilde{\sigma}^{\mathrm{L/R}}\mathbf{e}_\eta$. It turns out that this depends entirely on the problem and the boundary conditions one wishes to apply. There are a number of scenarios that can occur in solid mechanics, depending on whether the solid is in contact with a vacuum or another solid. Selected idealised conditions shall be considered separately.

- *Solid in contact with another solid: 'stick' conditions*
  The 'stick' boundary conditions for two solid materials in contact is an idealised condition where at the interface the traction and velocity vectors are equal:

$$\tilde{\sigma}^{\mathrm{L}}\mathbf{e}_\eta = \tilde{\sigma}^{\mathrm{R}}\mathbf{e}_\eta, \quad \tilde{\mathbf{u}}^{\mathrm{L}} = \tilde{\mathbf{u}}^{\mathrm{R}}. \tag{20}$$

The solution at the boundary for each material is given by Eq. (19), with ξ differing in sign for each component depending on the position in relation to the contact. The first three equations provide relations for $\tilde{\mathbf{u}}^{\mathrm{L/R}}$ in terms of the state $\mathbf{U}^{\mathrm{L/R}}$ (or coefficients deduced from it) and $\tilde{\sigma}^{\mathrm{L/R}}\mathbf{e}_\eta$ for each component

$$\tilde{\mathbf{u}}^{\mathrm{L}} = \mathbf{u}^{\mathrm{L}} + \left(\frac{1}{\rho}\mathbf{Q}^{-1}\mathcal{D}^{-1}\mathbf{Q}\right)^{\mathrm{L}}(\tilde{\sigma}^{\mathrm{L}} - \sigma^{\mathrm{L}})\mathbf{e}_\eta, \tag{21a}$$

$$\tilde{\mathbf{u}}^{\mathrm{R}} = \mathbf{u}^{\mathrm{R}} - \left(\frac{1}{\rho}\mathbf{Q}^{-1}\mathcal{D}^{-1}\mathbf{Q}\right)^{\mathrm{R}}(\tilde{\sigma}^{\mathrm{R}} - \sigma^{\mathrm{R}})\mathbf{e}_\eta. \tag{21b}$$

Substituting the conditions in Eq. (20) in Eq. (21) and rearranging gives

$$\tilde{\sigma}^{\mathrm{L/R}}\mathbf{e}_\eta = \left[\frac{1}{\rho^{\mathrm{L}}}\left(\mathbf{Q}^{-1}\mathcal{D}^{-1}\mathbf{Q}\right)^{\mathrm{L}} + \frac{1}{\rho^{\mathrm{R}}}\left(\mathbf{Q}^{-1}\mathcal{D}^{-1}\mathbf{Q}\right)^{\mathrm{R}}\right]^{-1}\left[\frac{1}{\rho^{\mathrm{L}}}\left(\mathbf{Q}^{-1}\mathcal{D}^{-1}\mathbf{Q}\right)^{\mathrm{L}}\sigma^{\mathrm{L}}\mathbf{e}_\eta + \frac{1}{\rho^{\mathrm{R}}}\left(\mathbf{Q}^{-1}\mathcal{D}^{-1}\mathbf{Q}\right)^{\mathrm{R}}\sigma^{\mathrm{R}}\mathbf{e}_\eta + \xi(\mathbf{u}^{\mathrm{R}} - \mathbf{u}^{\mathrm{L}})\right]. \tag{22}$$

- *Solid in contact with another solid: 'slip' conditions*
  Another idealised interfacial condition for two solids in contact is the 'slip' condition where the normal stress and normal velocities are equal, whilst the tangential components of the traction vectors are zero. It is more convenient in terms of notation for this example to consider the case of $\eta = 1$:

$$\tilde{\sigma}^{\mathrm{L}}_{11} = \tilde{\sigma}^{\mathrm{R}}_{11}, \quad \tilde{\sigma}^{\mathrm{L}}_{12} = \tilde{\sigma}^{\mathrm{L}}_{13} = \tilde{\sigma}^{\mathrm{R}}_{12} = \tilde{\sigma}^{\mathrm{R}}_{13} = 0, \quad \tilde{u}^{\mathrm{L}}_1 = \tilde{u}^{\mathrm{R}}_1. \tag{23}$$

In the same way as with the 'stick' boundary conditions, one starts with Eq. (21) defined for both materials. In this case only the expressions for $\tilde{u}^{\mathrm{L}}_1$ and $\tilde{u}^{\mathrm{R}}_1$ are required since the only unknowns are $\tilde{\sigma}^{\mathrm{L}}_{11}$ and $\tilde{\sigma}^{\mathrm{R}}_{11}$:

$$\tilde{u}^{\mathrm{L}}_1 = u^{\mathrm{L}}_1 + \left(\frac{1}{\rho}\mathbf{Q}^{-1}\mathcal{D}^{-1}\mathbf{Q}\right)^{\mathrm{L}}_{1i}(\tilde{\sigma}^{\mathrm{L}}_{1i} - \sigma^{\mathrm{L}}_{1i}), \tag{24a}$$

$$\tilde{u}^{\mathrm{R}}_1 = u^{\mathrm{R}}_1 - \left(\frac{1}{\rho}\mathbf{Q}^{-1}\mathcal{D}^{-1}\mathbf{Q}\right)^{\mathrm{R}}_{1i}(\tilde{\sigma}^{\mathrm{R}}_{1i} - \sigma^{\mathrm{R}}_{1i}). \tag{24b}$$

Setting the tangential components of the traction to zero and rearranging Eq. (24) gives

$$\tilde{\sigma}^{\mathrm{L/R}}_{11} = \left[\frac{1}{\rho^{\mathrm{L}}}\left(\mathbf{Q}^{-1}\mathcal{D}^{-1}\mathbf{Q}\right)^{\mathrm{L}}_{11} + \frac{1}{\rho^{\mathrm{R}}}\left(\mathbf{Q}^{-1}\mathcal{D}^{-1}\mathbf{Q}\right)^{\mathrm{R}}_{11}\right]^{-1}\left[\frac{1}{\rho^{\mathrm{L}}}\left(\mathbf{Q}^{-1}\mathcal{D}^{-1}\mathbf{Q}\right)^{\mathrm{L}}_{1i}\sigma^{\mathrm{L}}_{1i} + \frac{1}{\rho^{\mathrm{R}}}\left(\mathbf{Q}^{-1}\mathcal{D}^{-1}\mathbf{Q}\right)^{\mathrm{R}}_{1i}\sigma^{\mathrm{R}}_{1i} + u^{\mathrm{R}}_1 - u^{\mathrm{L}}_1\right]. \tag{25}$$

- *Solid in contact with a vacuum*
  A solid in contact with a vacuum is the simplest of the scenarios. This case requires that the traction is zero. Thus the boundary conditions are the required result:

$$\tilde{\sigma}^{\mathrm{L/R}}\mathbf{e}_\eta = 0. \tag{26}$$

This completes the approximate solution of the Riemann problem for a solid in contact with either another solid or vacuum, one need only insert the computed traction vector found from one of the above into Eq. (19) to give the solution at the boundary, $\widetilde{\mathbf{W}}^{\mathrm{L/R}}$.

A final consideration is that the value of stress taken at the boundary is only a first-order approximation. Thus one evaluation of Eq. (19) does not necessarily enforce, for example, $\tilde{\sigma}^{\mathrm{L/R}}\mathbf{e}_\eta = 0$ for the solid/vacuum case. It is simple to evaluate Eq. (19) a small number of times to achieve the required result, for each iteration taking the value of $\mathbf{W}^{\mathrm{L/R}}$ inside the boundary to be the last known value of $\widetilde{\mathbf{W}}^{\mathrm{L/R}}$. Experience shows that doing so has only a small influence on the final result, but then makes little impact on the overall cost of the scheme since these solutions are sought in the small number of boundary cells.

5. Examples

5.1. 1-d initial value problems

To assess the performance of the numerical methods, initial value problems are chosen that involve three-dimensional deformations. Each case differs not only in perhaps initial conditions, but in the materials involved and the boundary conditions that are applied at the interface. In respect to the latter, the one-dimensional tests are sufficient to asses the implementation of both stick and slip interfacial boundary conditions provided the problem is initialised to assume tangential components of velocity and/or traction. All computations are performed in the x_1-direction ($\eta = 1$).

To assess the performance of the numerical schemes for these problems, exact solutions have been found using the method proposed in [2]. The exact solution to a Riemann problem is uniquely determined from the (known) initial left and right states, and (unknown) wavespeeds. The residual error, $\mathcal{R}$, in continuity of, for example, the traction and velocities across the central contact as determined from the Rankine–Hugonoit and required boundary conditions, gives a measure of the error in the wavespeeds. The exact solution method follows an iterative procedure which given the initial left and right states seeks the exact wave speeds so as to minimise $\mathcal{R}$. The residuals are found by systematically evaluating the solution across each wave to obtain the inner most states either side of the contact. These states then provide the required measures. An initial guess of the wavespeeds, and of course wave types, is taken from an estimate of the inner states between waves using the linearised solver. The exact wavespeeds are then found by solving the non-linear system $\mathcal{R}(S_1, S_2, \ldots, S_6) = 0$ for $S_j, 1 \leqslant j \leqslant 6$, using the Newton–Raphson method. The way in which the solution is sought, by evaluating first the waves on the left side of the contact, and then for the right, make it straightforward to solve systems where the left and right materials differ, or in the case of solid/vacuum where material on one side does not exist.

5.1.1. Solid/solid 'stick' problem

In this first testcase both materials are considered to be copper with the parameters in the equation of state, Eq. (2), given in Table 1. The initial left and right velocities, deformation gradients, and entropies are taken to be:

$$\mathbf{U}^{\mathrm{L}}\left\{\begin{array}{l}\mathbf{u} = \begin{pmatrix} 2 \\ 0 \\ 0.1 \end{pmatrix} \text{ km s}^{-1}, \quad \mathbf{F} = \begin{pmatrix} 1 & 0 & 0 \\ -0.01 & 0.95 & 0.02 \\ -0.015 & 0 & 0.9 \end{pmatrix}, \quad S = 0 \text{ kJ g}^{-1}\text{ K}^{-1}, \\ \mathbf{U}^{\mathrm{R}}\left\{\begin{array}{l}\mathbf{u} = \begin{pmatrix} 0 \\ -0.03 \\ -0.01 \end{pmatrix} \text{ km s}^{-1}, \quad \mathbf{F} = \begin{pmatrix} 1 & 0 & 0 \\ 0.015 & 0.95 & 0 \\ -0.01 & 0 & 0.9 \end{pmatrix}, \quad S = 0 \text{ kJ g}^{-1}\text{ K}^{-1}. \end{array}\right. \end{array}\right.$$

These are the initial conditions used in [2], which were a modification of the testcase in [20]. The stick interfacial boundary conditions are used. This configuration is equivalent to a single material problem and thus provides an opportunity to assess the performance of the interface tracked scheme against a single material computation. A uniform grid is employed in the range [0:1] cm with a grid spacing $\Delta x = 1/500$ cm. The interface is initially located at $x_0 = 0.5$ cm. The CFL number $C = 0.6$ was used. The solution comprises, in order from left to right, a left travelling longitudinal shock, transverse rarefaction, and transverse shock; the right travelling wavetypes are symmetric to the left.

As is expected the single material method (SMM) resolves the contact wave across a finite number of grid points (Fig. 3). Small errors are noticeable in the density and entropy, occurrences which are synonymous to the so called 'heating' errors

Table 1
Equation of state parameters.

Parameter	Value			Units
	Cu	Al	Steel	
ρ_0	8.93	2.71	8.03	g cm^{-3}
c_0	4.6	6.22	5.68	km s^{-1}
c_v	$3.9 \cdot 10^{-4}$	$9.0 \cdot 10^{-4}$	$5.0 \cdot 10^{-4}$	kJ g^{-1} K^{-1}
T_0	300	300	300	K
b_0	2.1	3.16	3.1	km s^{-1}
α	1.0	1.0	0.596	–
β	3.0	3.577	2.437	–
γ	2.0	2.088	1.563	–

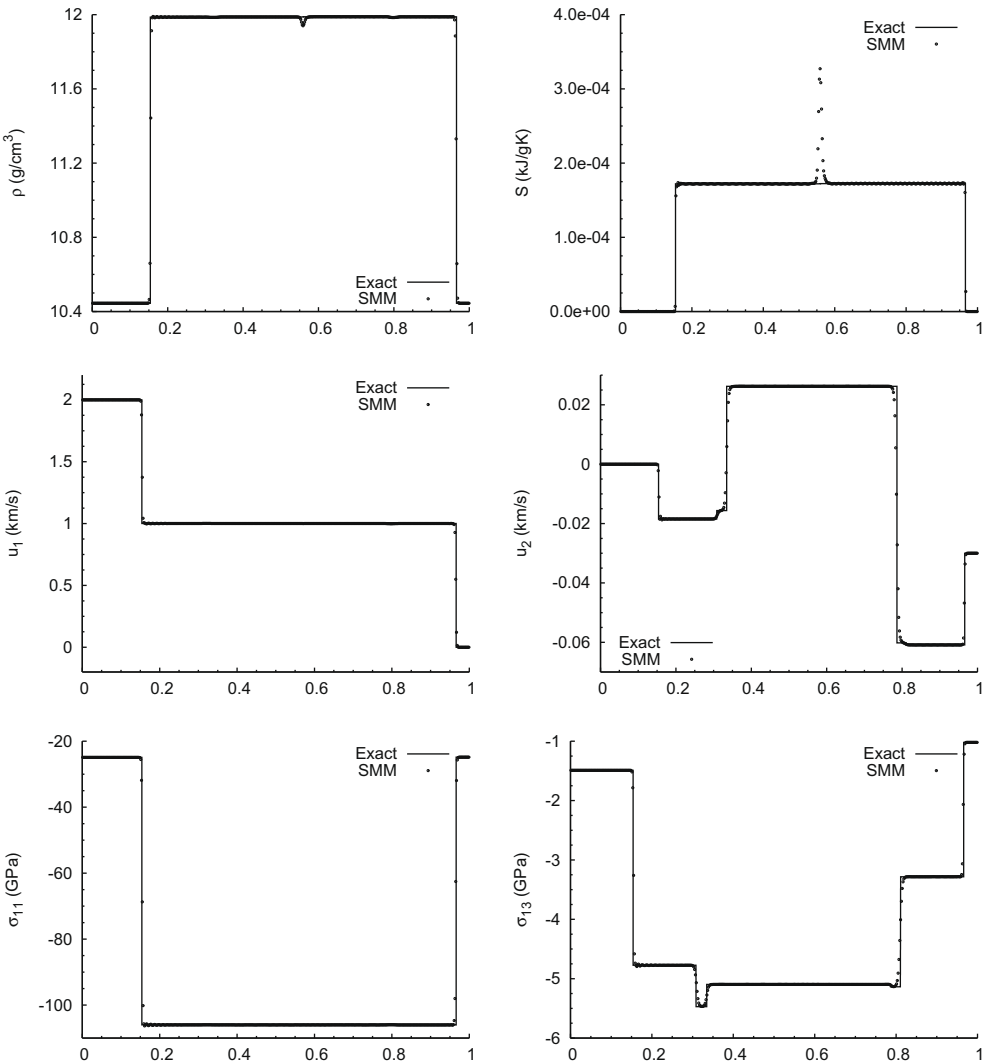

Fig. 3. Comparison of exact (solid line) and numerical (points) solutions for the solid/solid 'stick' testcase at the time $t = 0.6$ μs using the single material method (SMM), $C = 0.6$, and $\Delta x = 1/500$ cm.

observed in gas dynamics problems. The MGFM improves slightly on these errors (particularly observable in the entropy profile) and, as expected, maintains a sharp jump in variables across the contact (Fig. 4). The heating errors are largely reduced by applying the entropy fix (Fig. 5), in particular the undershoot in density is rendered obsolete and the large overshoots observed in entropy are somewhat suppressed. The resolution of non-linear wave profiles differs very little between each of the methods; the new multi-material method appears not to interfere with the performance of capturing non-linear waves achieved using the single material method in terms of monotonicity and diffusivity. All demonstrate excellent agreement of jump profiles and wavespeeds with the exact solution.

L_1-errors and convergence orders of selected variables are tabulated in Table 2 for different grid sizes and variants of the numerical method (here 1st-order refers to both space and time discretisation, and the 3rd-order WENO method is from [10] and uses the 3rd-order TVD RK method for time integration). It is mentioned that orders of convergence are not expected to exceed unity on account of the discontinuities present in the solution: for the L_1 norm, in the limit of very fine grids the error can converge no faster than Δx, hence, since solutions are always smeared over some finite number of grid points across discontinuities, the order is not expected to exceed unity regardless of the actual accuracy of the scheme in regions of smooth flow [33]. Nonetheless the error analysis provides a further means of justifying the high-order WENO-5 component of the proposed scheme. It is seen that for the normal velocity, which undergoes only small jumps between the left and right travelling longitudinal shocks, the orders differ little between each of the schemes. Although the WENO-5 method does improve on the observed errors, one cannot say that these values would be vastly non-achievable using even the 1st-order method with a refined mesh. However when the errors and orders of the tangential velocity u_3 and deformation gradient F_{21} are considered, the benefits of the WENO-5 variant become much more apparent. For these variables, the orders are some-

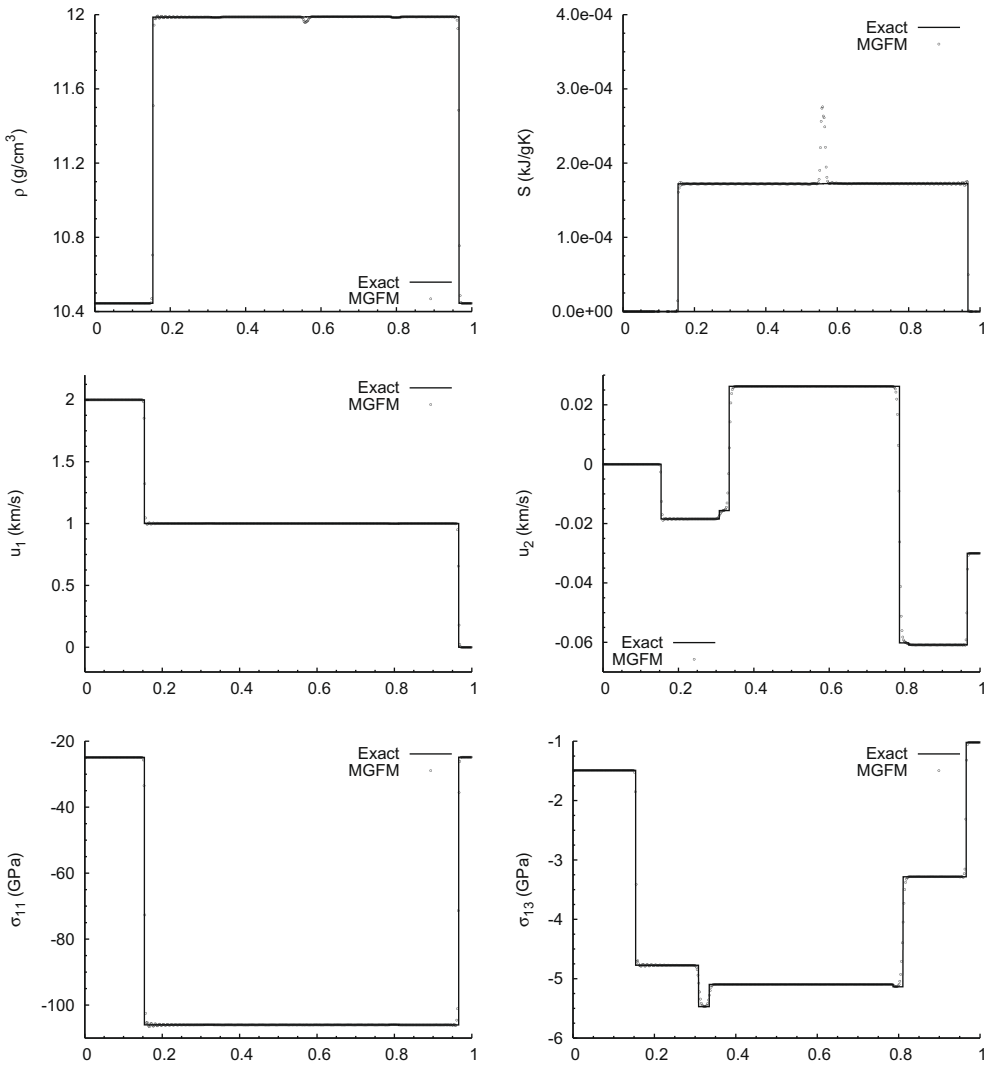

Fig. 4. Comparison of exact (solid line) and numerical (points) solutions for the solid/solid 'stick' testcase at the time $t = 0.6$ μs using the modified ghost fluid method (MGFM), $C = 0.6$, and $\Delta x = 1/500$ cm.

what higher and closer to unity, and the errors on the coarsest grid are lower than those for the 1st-order method using the finest mesh and the WENO-3 method using the medium grid. Thus, despite being almost an order of magnitude slower than the 1st-order method, the WENO-5 method is justified in terms of accuracy and cost when the resolution of the tangential waves is deemed important.

A further examination of the errors and orders of convergence is useful to compare the performance of the scheme with and without the entropy fix, and values are tabulated in Table 3. The observed visual impact of the entropy fix, in reducing the heating errors, is reflected in the lower errors found for the coarse grid; in particular for the density which is largely effected. However, as the grid is refined it is seen that the entropy fix becomes ineffective. In fact, the solution on finer grids without the fix yields smaller errors in comparison; the entropy fix appearing to marginally degrade the solution. Hence, convergence orders are slightly higher in almost all variables without the entropy fix. The employed finer grids may, however, be an unreasonable density for solving problems in multi-dimensions given the complexity of the governing equations, hence the entropy fix would prove to be a useful tool for more practical simulations.

5.2. Solid/solid 'slip' problem

In this example the left hand material is taken to be aluminium, whilst the right is copper. The necessary constants for both materials are given in Table 1. The initial states for the aluminium and copper are taken to be the same as the left and right states respectively for the solid/solid 'stick' problem. In this case however the slip boundary conditions were used in the interface calculation. This testcase thus enables the performance of the scheme to be assessed in the face of dissimilar

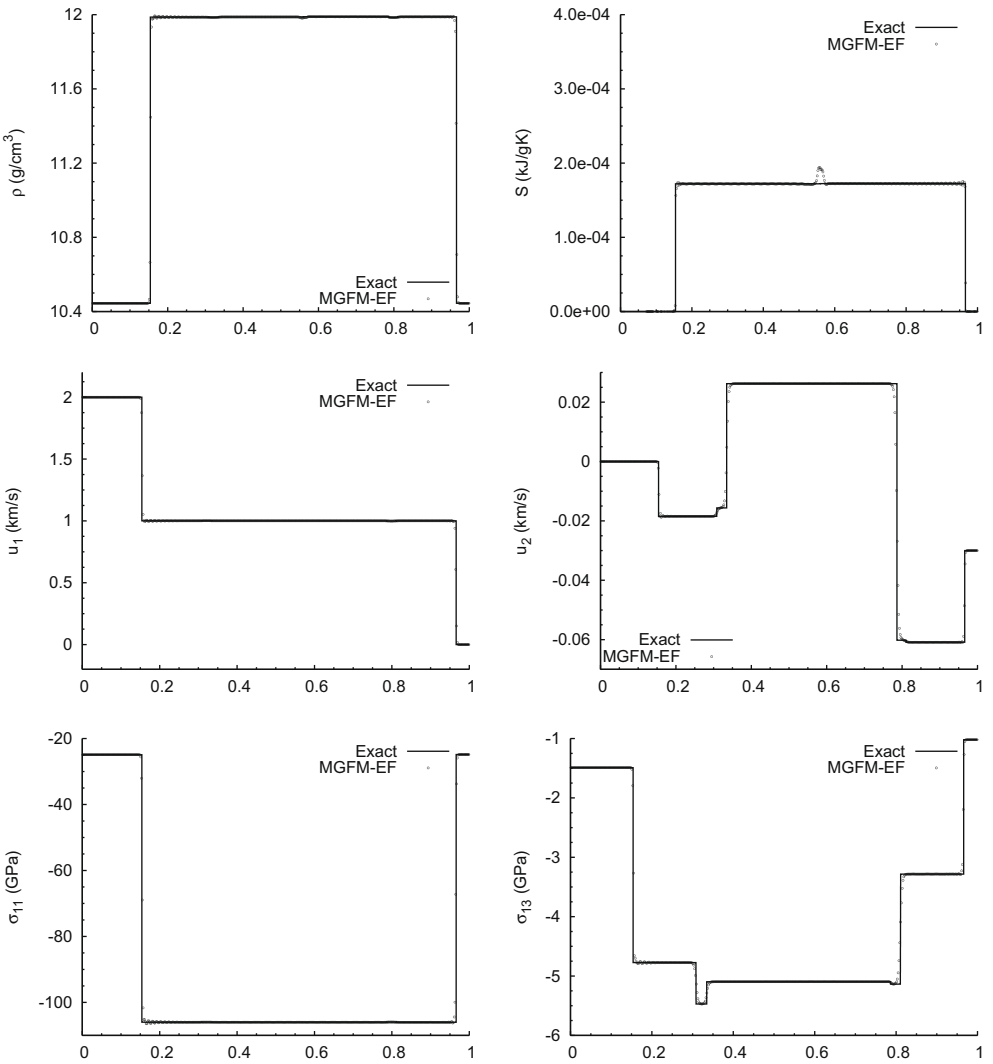

Fig. 5. Comparison of exact (solid line) and numerical (points) solutions for the solid/solid 'stick' testcase at the time $t = 0.6$ μs using the modified ghost fluid method with entropy fix (MGFM-EF), $C = 0.6$, and $\Delta x = 1/500$ cm.

Table 2
L_1 Errors and orders of convergence for the solid/solid 'stick' testcase: comparison of reconstruction schemes.

Scheme	N	u_1		u_3		F_{21}	
		L_1 Error	L_1 Order	L_1 Error	L_1 Order	L_1 Error	L_1 Order
1st Order	500	$3.172 \cdot 10^{-3}$	–	$9.118 \cdot 10^{-4}$	–	$4.183 \cdot 10^{-4}$	–
	1000	$1.621 \cdot 10^{-3}$	0.969	$6.440 \cdot 10^{-4}$	0.502	$2.937 \cdot 10^{-4}$	0.510
	2000	$7.931 \cdot 10^{-4}$	1.031	$4.399 \cdot 10^{-4}$	0.550	$2.076 \cdot 10^{-4}$	0.501
WENO3	500	$3.019 \cdot 10^{-3}$	–	$4.296 \cdot 10^{-4}$	–	$1.795 \cdot 10^{-4}$	–
	1000	$1.546 \cdot 10^{-3}$	0.966	$2.620 \cdot 10^{-4}$	0.714	$1.074 \cdot 10^{-4}$	0.740
	2000	$7.672 \cdot 10^{-4}$	1.010	$1.467 \cdot 10^{-4}$	0.837	$6.365 \cdot 10^{-5}$	0.756
WENO5	500	$2.237 \cdot 10^{-3}$	–	$2.615 \cdot 10^{-4}$	–	$1.072 \cdot 10^{-4}$	–
	1000	$1.139 \cdot 10^{-3}$	0.974	$1.537 \cdot 10^{-4}$	0.766	$5.946 \cdot 10^{-5}$	0.851
	2000	$5.865 \cdot 10^{-4}$	0.958	$8.120 \cdot 10^{-5}$	0.921	$3.272 \cdot 10^{-5}$	0.862

immiscible materials separated by an interface across which the materials should be allowed to slide freely. A uniform grid was employed in the range [0:1] cm with a grid spacing $\Delta x = 1/500$ cm. The interface is initially located at $x_0 = 0.5$ cm. The CFL number $C = 0.6$ was used. Under these conditions all six resultant non-linear waves in the solution are shocks: three left

Table 3
L_1 Errors and orders of convergence for the solid/solid 'stick' testcase: comparison with (EF) and without (NEF) the entropy fix.

Scheme	N	ρ		u_3		F_{21}	
		L_1 Error	L_1 Order	L_1 Error	L_1 Order	L_1 Error	L_1 Order
NEF	500	$4.024 \cdot 10^{-3}$	–	$2.615 \cdot 10^{-4}$	–	$1.072 \cdot 10^{-4}$	–
	1000	$2.060 \cdot 10^{-3}$	0.966	$1.537 \cdot 10^{-4}$	0.767	$5.946 \cdot 10^{-5}$	0.851
	2000	$1.038 \cdot 10^{-4}$	0.989	$8.120 \cdot 10^{-5}$	0.921	$3.272 \cdot 10^{-5}$	0.862
EF	500	$3.713 \cdot 10^{-3}$	–	$2.612 \cdot 10^{-4}$	–	$1.076 \cdot 10^{-4}$	–
	1000	$1.967 \cdot 10^{-3}$	0.916	$1.547 \cdot 10^{-4}$	0.756	$5.957 \cdot 10^{-5}$	0.853
	2000	$1.066 \cdot 10^{-4}$	0.985	$8.486 \cdot 10^{-5}$	0.867	$3.309 \cdot 10^{-5}$	0.848

travelling shocks in the aluminium and three right travelling in the copper. It is mentioned that the difference in material properties means that the waves propagate faster within the aluminium. The contact wave separating the two components moves to the right.

The space occupied by each of the materials is clear from the large change in density between each component across the interface which exhibits no smearing as expected. The heating errors observed previously without the entropy fix still manifest in the vicinity of the interface in the entropy profile (Fig. 6), although not as discernible in the density profile as a result of the large difference in material properties. The entropy fix again proves effective in suppressing these anomalies (Fig. 7), although not entirely eliminating the errors. Use of the fix again does not interfere with the

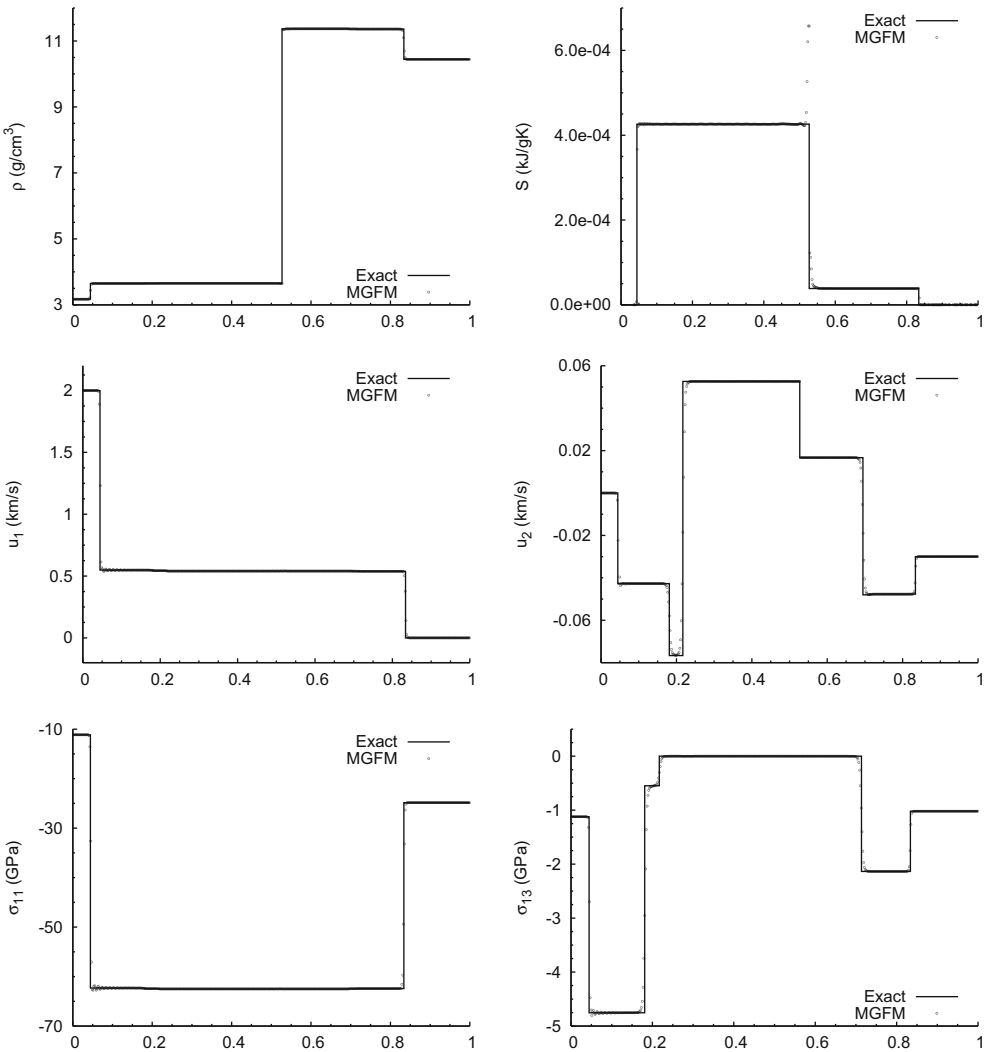

Fig. 6. Comparison of exact (solid line) and numerical (points) solutions of the solid/solid 'slip' testcase at the time $t = 0.5$ μs using the modified ghost fluid method (MGFM), $C = 0.6$, and $\Delta x = 1/500$ cm.

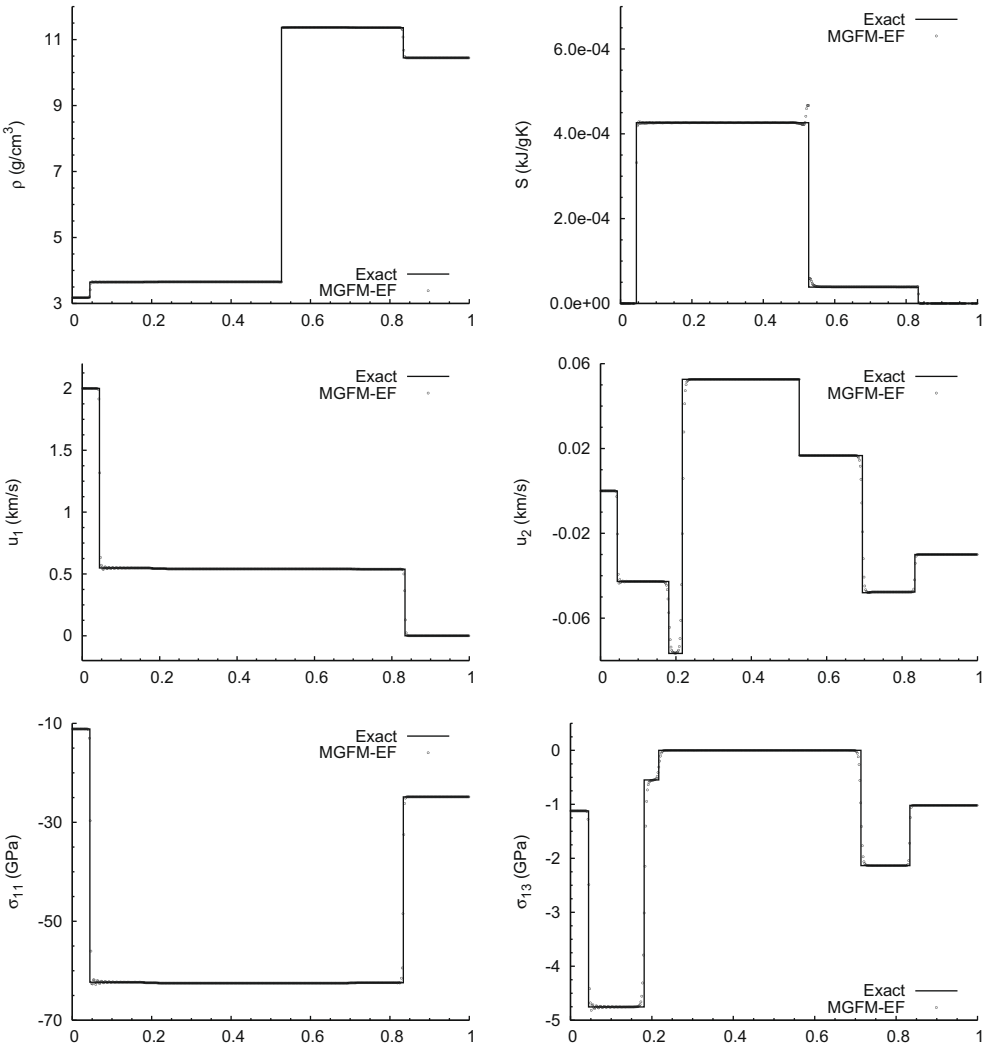

Fig. 7. Comparison of exact (solid line) and numerical (points) solutions of the solid/solid 'slip' testcase at the time $t = 0.5$ μs using the modified ghost fluid method with entropy fix (MGFM-EF), $C = 0.6$, and $\Delta x = 1/500$ cm.

resolving of non-linear waves; the waves being captured over a similar finite number of grid points. Contrary to the previous example, tangential components of velocity and stress undergo much larger jumps across the transverse waves in the aluminium as a result of the different material properties and relief of traction at the interface. The high-order scheme nonetheless proves effective in resolving these delicate features, albeit across a much larger number of cells in comparison to the longitudinal waves.

An important feature desirable from the proposed scheme is the ability to accurately model compressible solids on fixed grids with relative slide. In this example using the slip boundary condition this should certainly be the case. Considering again at the tangential velocity and stress profiles, it is observed that in comparison to the exact solution, the slip boundary conditions are accurately enforced and excellent agreement is achieved in the discontinuous change across the interface. Despite the interface having moved across a finite number of cells there is no apparent transfer of tangential momentum, the materials slide freely over one another, and the tangential components of the traction go to zero across the contact wave.

5.3. Solid/vacuum problem

This final one-dimensional example assumes only the left hand material is solid; the initial contact, located at $x_0 = 0.5$ cm, is a free-surface of the semi-infinite solid and the right hand region taken to be a vacuum. The solid material is aluminium

with constants tabulated in Table 1. The initial conditions are taken from those of the left material of the previous solid/solid testcases:

$$\mathbf{u} = \begin{pmatrix} 2 \\ 0 \\ 0.1 \end{pmatrix} \text{km s}^{-1}, \quad \mathbf{F} = \begin{pmatrix} 1 & 0 & 0 \\ -0.01 & 0.95 & 0.02 \\ -0.015 & 0 & 0.9 \end{pmatrix}, \quad S = 0 \text{ kJ g}^{-1} \text{ K}^{-1}.$$

As in the previous examples a uniform grid was employed in the range [0:1] cm with a grid spacing $\Delta x = 1/500$ cm, and the CFL number taken to be $C = 0.6$. The solution comprises a longitudinal rarefaction wave followed by two transverse shock waves all propagating to the left of the initial contact. The initial state of the solid results in an acceleration of the free-surface (contact) to the right.

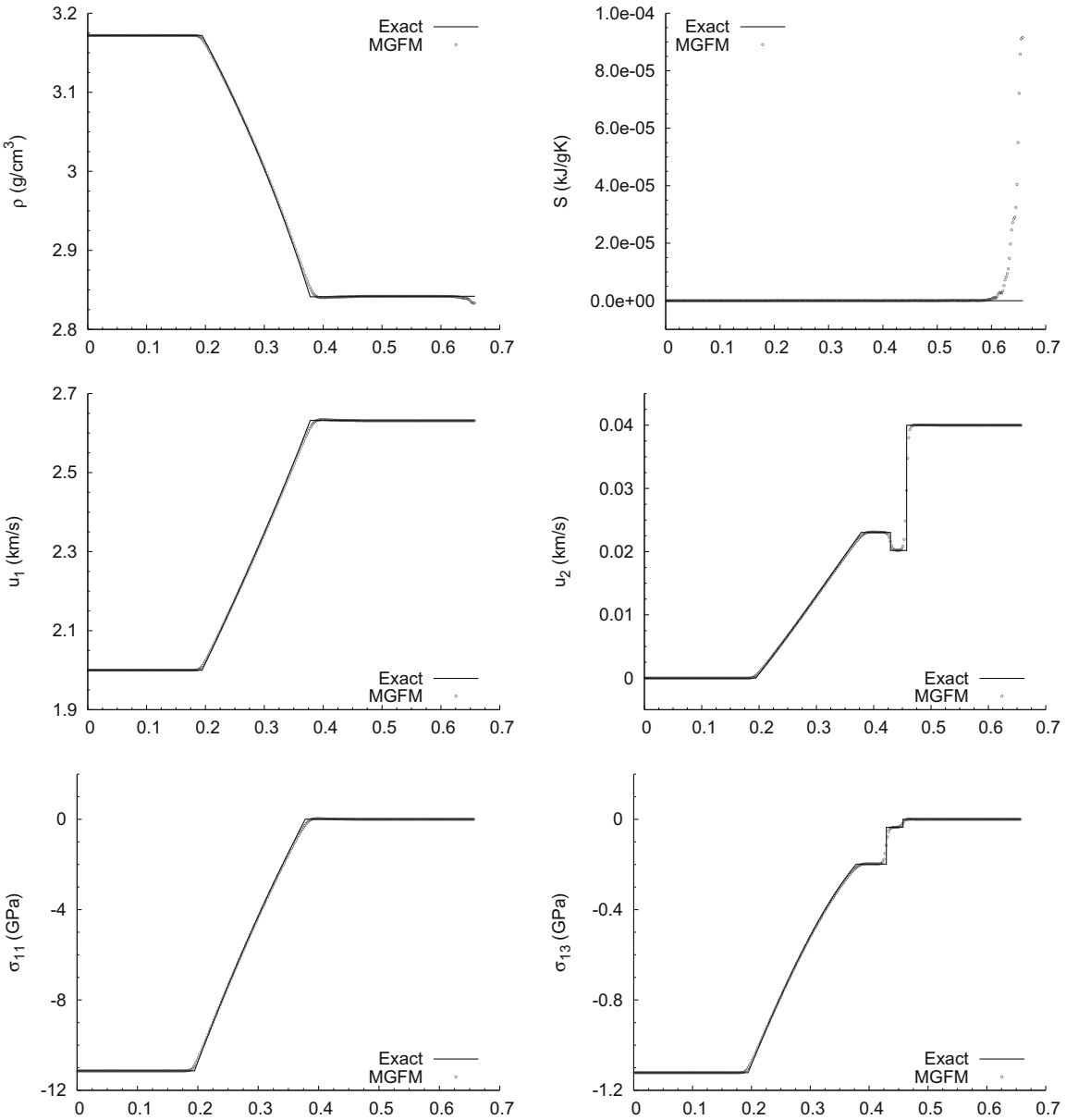

Fig. 8. Comparison of exact (solid line) and numerical (points) solutions for the solid/vacuum testcase at the time $t = 0.6$ μs using the modified ghost fluid method (MGFM), $C = 0.6$, and $\Delta x = 1/500$ cm.

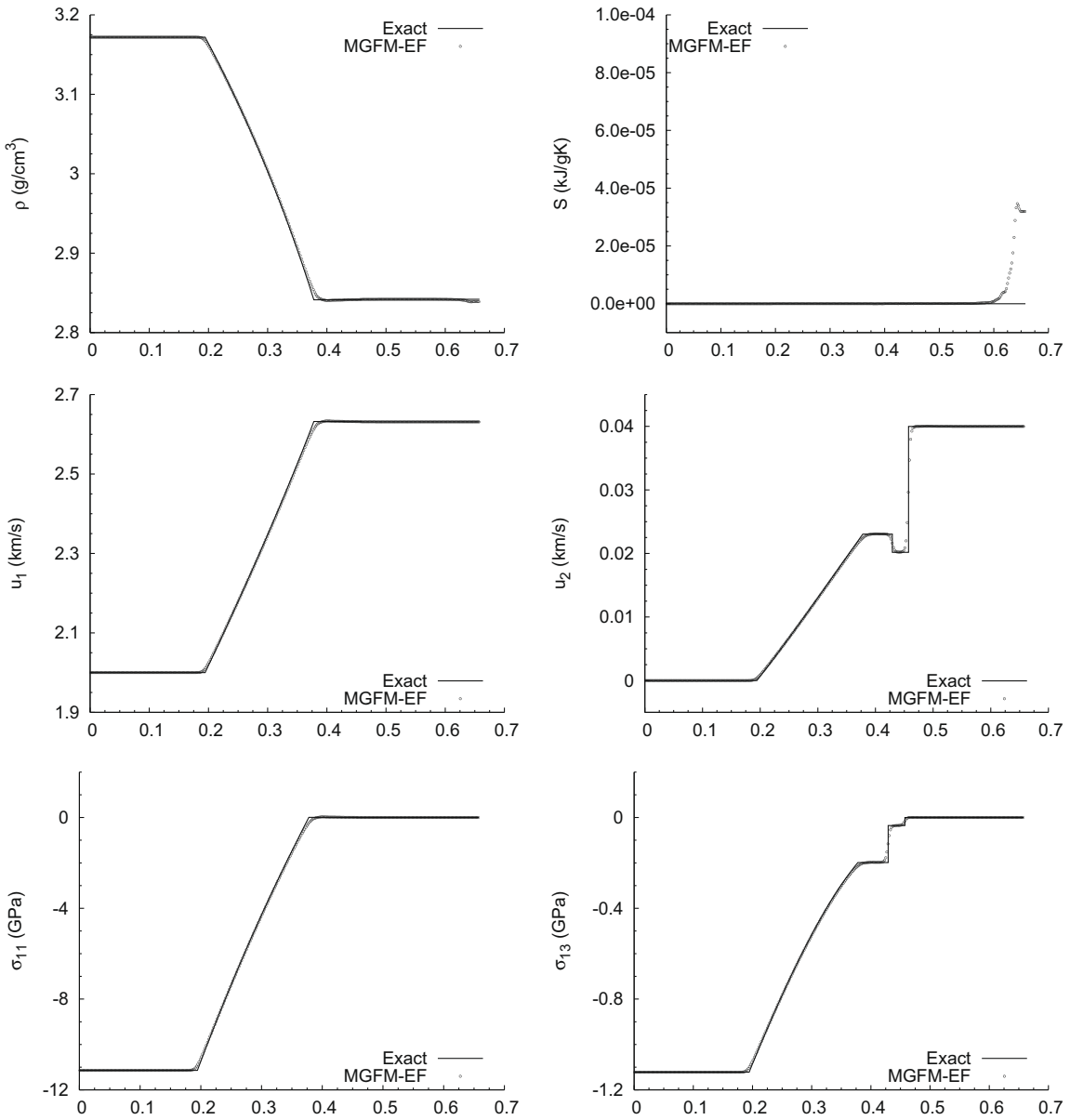

Fig. 9. Comparison of exact (solid line) and numerical (points) solutions for the solid/vacuum testcase at the time $t = 0.6$ μs using the modified ghost fluid method with entropy fix (MGFM-EF), $C = 0.6$, and $\Delta x = 1/500$ cm.

It is expected in this case that the acceleration of the interface is accompanied by a relief of the traction of the free-surface, which should see all components go to zero. As in the previous examples the numerical solutions are investigated without (Fig. 8) and with (Fig. 9) the entropy fix. Both variations of the multi-material method are successful in achieving the zero traction boundary condition and predicting accurate locations of the non-linear waves and free-surface. In this case the unbounded free-surface moves a considerable distance by comparison and it can be seen that this has no impact on the excellent agreement of the numerically predicted final interface location in comparison to the exact. However, similar behaviour as in the previous testcases are observed of heating errors in the vicinity of the contact surface. An undershoot in density and prominent overshoot in entropy for the variant without the fix is found, the number of grid points affected by the heating error in the entropy profile appears to exceed that seen previously. The addition of the entropy fix renders the density heating errors almost obsolete, but only mildly suppresses the entropy error. Despite these errors, the traction goes to zero and overall profiles are in good agreement with the exact solutions.

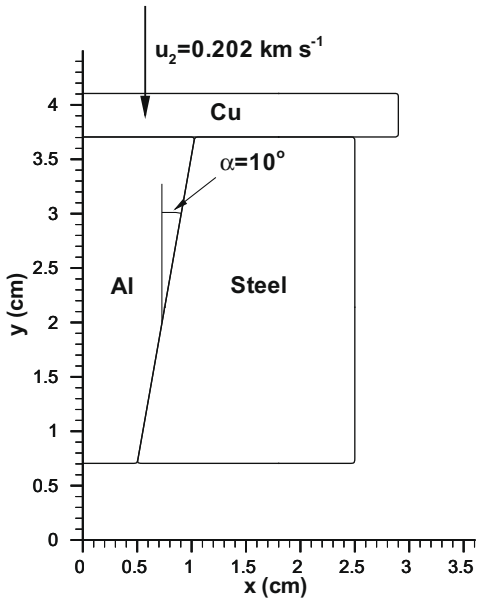

Fig. 10. Illustration of the friction experiment setup.

5.4. 2-d example

In the final example the scheme is demonstrated in two-dimensions by simulating the experimental setup from [12] of a copper flyer plate impacting an aluminium cone encased within a steel shroud (Fig. 10). Although only non-linear elastic solids are considered in the present study, and indeed in reality inelastic deformations will play a role, this test-case provides an opportunity to assess the ability to allow for sliding in two-dimensions. Material properties for all components are tabulated in Table 1. The problem is cylindrically symmetric, hence the governing laws are augmented by the geometric source terms presented in [3]. Each material is identifiable by a dedicated level-set function, with the surrounding space taken to be a vacuum. The use of multiple level-set fields within a void calls for the inclusion of some form of collision criteria, such that the contact between each material is identifiable within each cell. Here the approach proposed in [29] is used where contact between a Solid 1 and Solid 2 is assumed whenever the difference in level-set fields between the two materials is less than 10% of the cell size: $|\phi^{S1} + \phi^{S2}| < 0.1\Delta x \rightarrow$ contact. The computational grid covered the domain $[0{:}3.6, 0{:}4.28]$ cm, with uniform quadrilateral cells of size $\Delta\mathbf{x} = 1/50$ cm. The CFL number was taken to be $C = 1/3$. For the initial conditions all materials are assumed to be in a stress free configuration: $\mathbf{F} = \mathbf{I}$ and $S = 0$. The cone and steel casing were taken to be at rest, whilst the copper flyer plate was initialised with a non-zero velocity component: $u_2 = 0.202$ km s^{-1} for solutions sought in x_1x_2-domain. Solutions were computed for both the slip and stick boundary conditions. For the former this experiment proves to be a rigorous test on account of the interface between the aluminium cone and steel casing lying at an oblique angle to the Cartesian coordinate system; thus the experiment provides analysis of the ability to allow for sliding in higher-dimensions.

The impact of the copper plate results in a shock wave propagating into the cone and case wave travels obliquely to the interface (Fig. 11). Likewise a shock propagates into the flyer plate, which, upon reaching the upper free-surface, results in a downwards moving elastic release wave. The fact that the waves propagate at an angle to the interface between the cone and case means a discontinuous change occurs in the component of velocity tangential to the boundary, and hence sliding between the two components, in the case of slip conditions. Upon reaching the bottom free-surface of the cone in this case, the initial shock wave forces the cone to protrude from the confining case. The stick boundary conditions on the other hand result in no sliding and thus the bottom free-surface of the cone and case move simultaneously following the arrival of the first wave. The prominent influence of the chosen interfacial boundary conditions is illustrated by the markedly different time-histories of free-surface velocity of the central cone and casing (Fig. 12). Due to the difference in material properties, the waves travel faster in the aluminium cone than the steel case. Thus, the initial shock reaches the free-surface of the cone some time before reaching the free-surface of the case. For the slip boundary conditions the shock accelerates the free-surface of the cone which subsequently maintains a constant velocity until arrival of the release wave. For the stick conditions, the free-surface of the case is initially accelerated but quickly decelerates due to the binding to the (at that point in time) stationary case. Only once the loading shock has reached the case free-surface does the cone begin again to accelerate further. Referring back to 1,

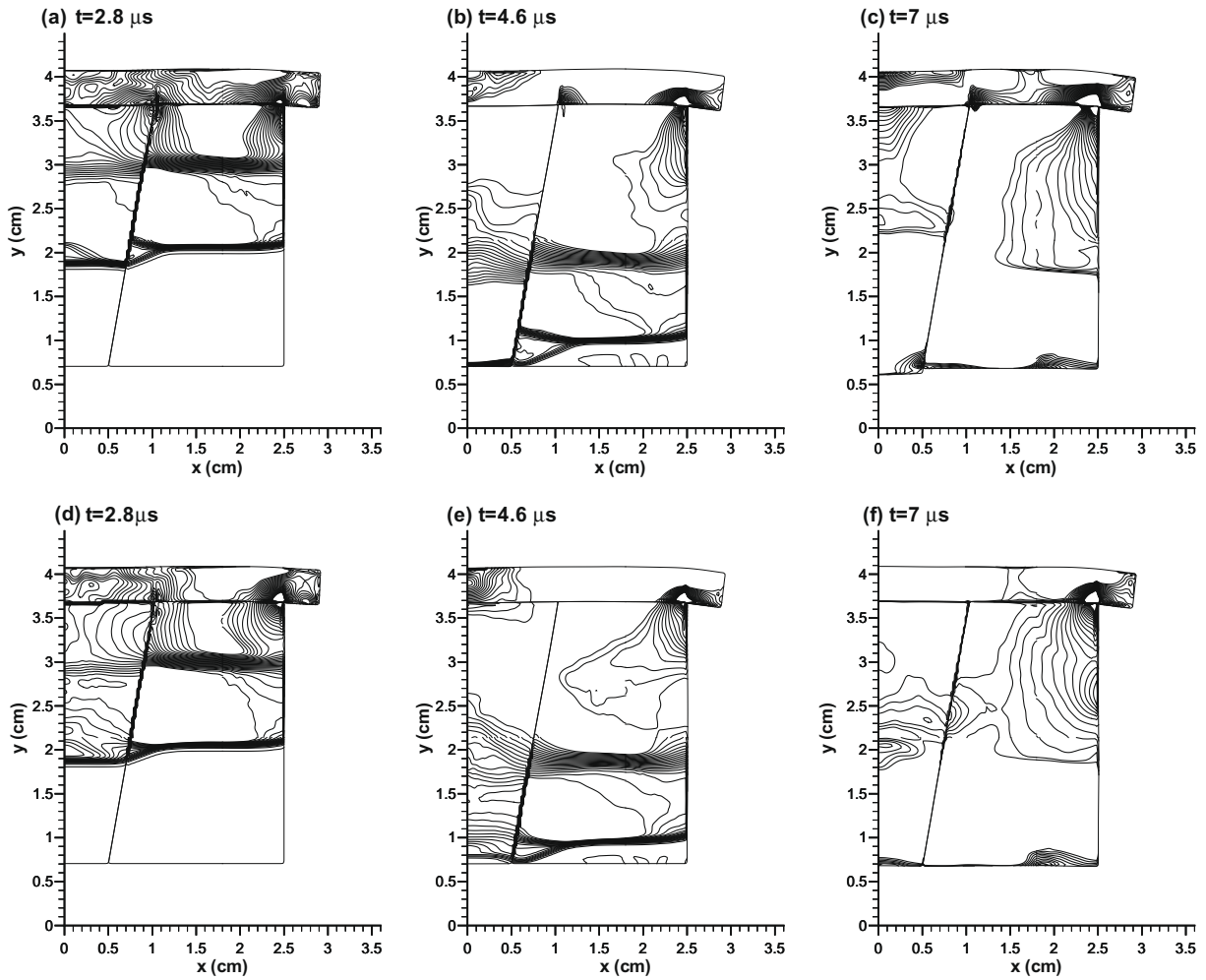

Fig. 11. Contour plots of the pressure, $p = -\mathrm{Tr}(\sigma)/3$, at different indicated times for the friction experiment using (a)–(c) the slip boundary conditions, and (d)–(f) the stick boundary conditions.

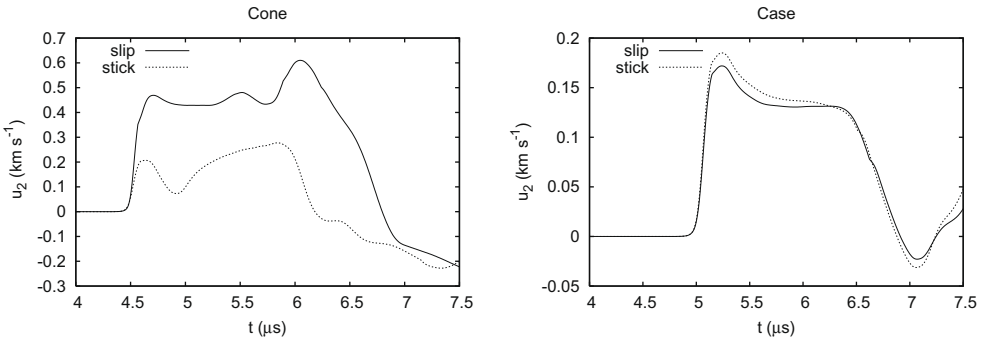

Fig. 12. Time evolution of free-surface velocities for the aluminium cone and steel case showing the effects of using the stick and slip interfacial boundary conditions. Measurements were taken at the radial locations $x = 0$ cm and $x = 1.5$ cm of the free-surfaces for the cone and case respectively.

in reality one would expect that the interfacial friction would dictate that the behaviour lie somewhere between these two results. It is thus encouraging that the present method successfully realises both the bounding limits of interfacial motion.

6. Conclusions

The modified ghost fluid method originally applied to the equations of gas-dynamics has been extended to non-linear elastic materials in multi-dimensions. The method boasts the use of fixed Cartesian grids and high-order shock capturing methods whilst maintaining sharp interfaces and a simple means to employ existing single component solvers to capture interface interactions. The required solution of multi-material Riemann problems has been derived for different interfacial boundary conditions including a solid in contact with anther solid, and a solid in contact with a vacuum. The scheme is a straightforward extension of an existing high-order single material method. Level-set functions are employed to allow the possibility of relative sliding between solid components. Numerical solutions of various multi-material problems demonstrates an accurate incorporation of each boundary condition. A particularly favourable achievement is the ability to allow perfect sliding.

The focus of this paper has been non-linear elastic solids, but some remarks should be made about possible extension of the scheme to include inelastic deformations and the effects of this additional physics. Inclusion of elastoplastic deformations, for example, will result in reduced stresses in some cases but perhaps larger deformations. In [3] it was shown that the resulting inhomogeneous system can be solved using time operator splitting, thus requiring no change to the underlying solution of the equations for non-linear elasticity. Since plastic deformations are volume preserving these have no influence on the boundary evolution. Thus it should be possible to include inelastic deformations by means of modifications made only to the underlying single material solver.

Acknowledgements

The financial support from the Engineering and Physical Sciences Research Council (EP/D051940/1) and the MoD-AWE Joint Grant Scheme (JGS 607) is greatly appreciated. The authors benefitted from conversations with Evgeniy Romenski. PTB would also like to thank Anatoly Resnyansky for providing equation of state parameters for aluminium.

Appendix A. Characteristic decomposition

In quasi-linear form the system Eq. (1) reduces to

$$\frac{\partial \mathbf{W}}{\partial t} + \mathcal{A}^{\eta} \frac{\partial \mathbf{W}}{\partial x_{\eta}} = 0, \tag{A.1}$$

where

$$\mathbf{W} = \left(\mathbf{u}, \mathbf{F}^{\mathrm{T}}\mathbf{e}_1, \mathbf{F}^{\mathrm{T}}\mathbf{e}_2, \mathbf{F}^{\mathrm{T}}\mathbf{e}_3, S\right) \tag{A.2}$$

is the vector of primitive variables, and the Jacobian matrix is:

$$\mathcal{A}^{\eta} = \begin{pmatrix} u_{\eta}\mathbf{I} & -\mathbf{A}^{\eta 1} & -\mathbf{A}^{\eta 2} & -\mathbf{A}^{\eta 3} & -\mathbf{B}^{\eta} \\ -\mathbf{F}^{\mathrm{T}}\mathbf{D}_{\eta 1} & u_{\eta}\mathbf{I} & 0 & 0 & 0 \\ -\mathbf{F}^{\mathrm{T}}\mathbf{D}_{\eta 2} & 0 & u_{\eta}\mathbf{I} & 0 & 0 \\ -\mathbf{F}^{\mathrm{T}}\mathbf{D}_{\eta 3} & 0 & 0 & u_{\eta}\mathbf{I} & 0 \\ 0 & 0 & 0 & 0 & u_{\eta} \end{pmatrix}, \tag{A.3}$$

where $\mathbf{D}_{ij} = \mathbf{e}_i \otimes \mathbf{e}_j^{\mathrm{T}}$ are the unit Dyads, $\mathbf{I}$ the identity matrix, and the following coefficients were used:

$$A_{ij}^{\eta k} = \frac{1}{\rho}\frac{\partial \sigma_{\eta i}}{\partial F_{kj}}, \quad B_i^{\eta} = \frac{1}{\rho}\frac{\partial \sigma_{\eta i}}{\partial S}. \tag{A.4}$$

Considering only the η-direction, the matrix Eq. (A.3) has the following eigenvalues (in canonical order):

$$\Lambda = \mathrm{diag}\left(u_{\eta}\mathbf{I} - \mathcal{D}, u_{\eta}\mathbf{I}, u_{\eta}\mathbf{I}, u_{\eta}, u_{\eta}\mathbf{I} + \pi\mathcal{D}\pi\right), \tag{A.5}$$

where

$$\pi = \begin{pmatrix} 0 & 0 & 1 \\ 0 & 1 & 0 \\ 1 & 0 & 0 \end{pmatrix},$$

and $\mathcal{D}^2$ is the diagonal matrix of eigenvalues of the symmetric positive definite *acoustic tensor* $\mathbf{\Omega} = [\Omega_{ij}]$:

$$\Omega_{ij} = A_{ik}^{\eta j} F_{\eta k} = \mathbf{Q}^{-1}\mathcal{D}^2\mathbf{Q}, \tag{A.6}$$

with $\mathbf{Q}$ an orthogonal matrix. Note that contrary to the employed notation the repeated η in Eq. (A.6) and in what follows refers to the direction and not summation over repeated indices. The matrix of left eigenvectors is:

$$\mathbf{L} = (\mathbf{l}_1, \mathbf{l}_2, \mathbf{l}_3, \mathbf{l}_4, \mathbf{l}_5, \mathbf{l}_6, \mathbf{l}_7, \mathbf{l}_8, \mathbf{l}_9, \mathbf{l}_{10}, \mathbf{l}_{11}, \mathbf{l}_{12}, \mathbf{l}_{13})^{\mathrm{T}}, \tag{A.7}$$

where

$$\mathbf{l}_1 = \Big((\mathcal{D}\mathbf{Q})_{11}, (\mathcal{D}\mathbf{Q})_{12}, (\mathcal{D}\mathbf{Q})_{13}, Q_{1i}A_{i1}^{\eta 1}, Q_{1i}A_{i2}^{\eta 1}, Q_{1i}A_{i3}^{\eta 1}, Q_{1i}A_{i1}^{\eta 2}, Q_{1i}A_{i2}^{\eta 2}, Q_{1i}A_{i3}^{\eta 2}, Q_{1i}A_{i1}^{\eta 3}, Q_{1i}A_{i2}^{\eta 3}, Q_{1i}A_{i3}^{\eta 3}, Q_{1i}B_i^{\eta}\Big),$$

$$\mathbf{l}_2 = \Big((\mathcal{D}\mathbf{Q})_{21}, (\mathcal{D}\mathbf{Q})_{22}, (\mathcal{D}\mathbf{Q})_{23}, Q_{2i}A_{i1}^{\eta 1}, Q_{2i}A_{i2}^{\eta 1}, Q_{2i}A_{i3}^{\eta 1}, Q_{2i}A_{i1}^{\eta 2}, Q_{2i}A_{i2}^{\eta 2}, Q_{2i}A_{i3}^{\eta 2}, Q_{2i}A_{i1}^{\eta 3}, Q_{2i}A_{i2}^{\eta 3}, Q_{2i}A_{i3}^{\eta 3}, Q_{2i}B_i^{\eta}\Big),$$

$$\mathbf{l}_3 = \Big((\mathcal{D}\mathbf{Q})_{31}, (\mathcal{D}\mathbf{Q})_{32}, (\mathcal{D}\mathbf{Q})_{33}, Q_{3i}A_{i1}^{\eta 1}, Q_{3i}A_{i2}^{\eta 1}, Q_{3i}A_{i3}^{\eta 1}, Q_{3i}A_{i1}^{\eta 2}, Q_{3i}A_{i2}^{\eta 2}, Q_{3i}A_{i3}^{\eta 2}, Q_{3i}A_{i1}^{\eta 3}, Q_{3i}A_{i2}^{\eta 3}, Q_{3i}A_{i3}^{\eta 3}, Q_{3i}B_i^{\eta}\Big),$$

$$\mathbf{l}_4 = (0,0,0,F_{\eta 2}/F_{\eta 1},-1,0,0,0,0,0,0,0,0),$$

$$\mathbf{l}_5 = (0,0,0,F_{\eta 3}/F_{\eta 1},0,-1,0,0,0,0,0,0,0),$$

$$\mathbf{l}_6 = (0,0,0,0,0,0,F_{\eta 2}/F_{\eta 1},-1,0,0,0,0,0),$$

$$\mathbf{l}_7 = (0,0,0,0,0,0,F_{\eta 3}/F_{\eta 1},0,-1,0,0,0,0),$$

$$\mathbf{l}_8 = (0,0,0,0,0,0,0,0,0,F_{\eta 2}/F_{\eta 1},-1,0,0),$$

$$\mathbf{l}_9 = (0,0,0,0,0,0,0,0,0,F_{\eta 3}/F_{\eta 1},0,-1,0),$$

$$\mathbf{l}_{10} = (0,0,0,0,0,0,0,0,0,0,0,0,1),$$

$$\mathbf{l}_{11} = \Big((\mathcal{D}\mathbf{Q})_{31}, (\mathcal{D}\mathbf{Q})_{32}, (\mathcal{D}\mathbf{Q})_{33}, -Q_{3i}A_{i1}^{\eta 1}, -Q_{3i}A_{i2}^{\eta 1}, -Q_{3i}A_{i3}^{\eta 1}, -Q_{3i}A_{i1}^{\eta 2}, -Q_{3i}A_{i2}^{\eta 2}, -Q_{3i}A_{i3}^{\eta 2}, -Q_{3i}A_{i1}^{\eta 3}, -Q_{3i}A_{i2}^{\eta 3}, -Q_{3i}A_{i3}^{\eta 3}, -Q_{3i}B_i^{\eta}\Big),$$

$$\mathbf{l}_{12} = \Big((\mathcal{D}\mathbf{Q})_{21}, (\mathcal{D}\mathbf{Q})_{22}, (\mathcal{D}\mathbf{Q})_{23}, -Q_{2i}A_{i1}^{\eta 1}, -Q_{2i}A_{i2}^{\eta 1}, -Q_{2i}A_{i3}^{\eta 1}, -Q_{2i}A_{i1}^{\eta 2}, -Q_{2i}A_{i2}^{\eta 2}, -Q_{2i}A_{i3}^{\eta 2}, -Q_{2i}A_{i1}^{\eta 3}, -Q_{2i}A_{i2}^{\eta 3}, -Q_{2i}A_{i3}^{\eta 3}, -Q_{2i}B_i^{\eta}\Big),$$

$$\mathbf{l}_{13} = \Big((\mathcal{D}\mathbf{Q})_{11}, (\mathcal{D}\mathbf{Q})_{12}, (\mathcal{D}\mathbf{Q})_{13}, -Q_{1i}A_{i1}^{\eta 1}, -Q_{1i}A_{i2}^{\eta 1}, -Q_{1i}A_{i3}^{\eta 1}, -Q_{1i}A_{i1}^{\eta 2}, -Q_{1i}A_{i2}^{\eta 2}, -Q_{1i}A_{i3}^{\eta 2}, -Q_{1i}A_{i1}^{\eta 3}, -Q_{1i}A_{i2}^{\eta 3}, -Q_{1i}A_{i3}^{\eta 3}, -Q_{1i}B_i^{\eta}\Big).$$

and the matrix of right eigenvectors is:

$$\mathbf{R} = (\mathbf{r}_1, \mathbf{r}_2, \mathbf{r}_3, \mathbf{r}_4, \mathbf{r}_5, \mathbf{r}_6, \mathbf{r}_7, \mathbf{r}_8, \mathbf{r}_9, \mathbf{r}_{10}, \mathbf{r}_{11}, \mathbf{r}_{12}, \mathbf{r}_{13}), \tag{A.8}$$

where

$$\mathbf{r}_1 = \frac{1}{2}\Big((\mathcal{D}\mathbf{Q})_{11}^{-1}, (\mathcal{D}\mathbf{Q})_{21}^{-1}, (\mathcal{D}\mathbf{Q})_{31}^{-1}, F_{\eta 1}(\mathcal{D}^2\mathbf{Q})_{11}^{-1}, F_{\eta 2}(\mathcal{D}^2\mathbf{Q})_{11}^{-1}, F_{\eta 3}(\mathcal{D}^2\mathbf{Q})_{11}^{-1}, F_{\eta 1}(\mathcal{D}^2\mathbf{Q})_{21}^{-1}, F_{\eta 2}(\mathcal{D}^2\mathbf{Q})_{21}^{-1}, F_{\eta 3}(\mathcal{D}^2\mathbf{Q})_{21}^{-1}, F_{\eta 1}$$
$$(\mathcal{D}^2\mathbf{Q})_{31}^{-1}, F_{\eta 2}(\mathcal{D}^2\mathbf{Q})_{31}^{-1}, F_{\eta 3}(\mathcal{D}^2\mathbf{Q})_{31}^{-1}, 0\Big)^{\mathrm{T}},$$

$$\mathbf{r}_2 = \frac{1}{2}\Big((\mathcal{D}\mathbf{Q})_{12}^{-1}, (\mathcal{D}\mathbf{Q})_{22}^{-1}, (\mathcal{D}\mathbf{Q})_{32}^{-1}, F_{\eta 1}(\mathcal{D}^2\mathbf{Q})_{12}^{-1}, F_{\eta 2}(\mathcal{D}^2\mathbf{Q})_{12}^{-1}, F_{\eta 3}(\mathcal{D}^2\mathbf{Q})_{12}^{-1}, F_{\eta 1}(\mathcal{D}^2\mathbf{Q})_{22}^{-1}, F_{\eta 2}(\mathcal{D}^2\mathbf{Q})_{22}^{-1}, F_{\eta 3}(\mathcal{D}^2\mathbf{Q})_{22}^{-1}, F_{\eta 1}$$
$$(\mathcal{D}^2\mathbf{Q})_{32}^{-1}, F_{\eta 2}(\mathcal{D}^2\mathbf{Q})_{32}^{-1}, F_{\eta 3}(\mathcal{D}^2\mathbf{Q})_{32}^{-1}, 0\Big)^{\mathrm{T}},$$

$$\mathbf{r}_3 = \frac{1}{2}\Big((\mathcal{D}\mathbf{Q})_{13}^{-1}, (\mathcal{D}\mathbf{Q})_{23}^{-1}, (\mathcal{D}\mathbf{Q})_{33}^{-1}, F_{\eta 1}(\mathcal{D}^2\mathbf{Q})_{13}^{-1}, F_{\eta 2}(\mathcal{D}^2\mathbf{Q})_{13}^{-1}, F_{\eta 3}(\mathcal{D}^2\mathbf{Q})_{13}^{-1}, F_{\eta 1}(\mathcal{D}^2\mathbf{Q})_{23}^{-1}, F_{\eta 2}(\mathcal{D}^2\mathbf{Q})_{23}^{-1}, F_{\eta 3}(\mathcal{D}^2\mathbf{Q})_{23}^{-1}, F_{\eta 1}$$
$$(\mathcal{D}^2\mathbf{Q})_{33}^{-1}, F_{\eta 2}(\mathcal{D}^2\mathbf{Q})_{33}^{-1}, F_{\eta 3}(\mathcal{D}^2\mathbf{Q})_{33}^{-1}, 0\Big)^{\mathrm{T}},$$

$$\mathbf{r}_4 = \Big(0,0,0,F_{\eta 1}\Omega_{1i}^{-1}A_{i2}^{\eta 1}, F_{\eta 2}\Omega_{1i}^{-1}A_{i2}^{\eta 1} - 1, F_{\eta 3}\Omega_{1i}^{-1}A_{i2}^{\eta 1}, F_{\eta 1}\Omega_{1i}^{-1}A_{i2}^{\eta 1}F_{\eta 2}\Omega_{1i}^{-1}A_{i2}^{\eta 1}, F_{\eta 3}\Omega_{1i}^{-1}A_{i2}^{\eta 1}, F_{\eta 1}\Omega_{3i}^{-1}A_{i2}^{\eta 1}, F_{\eta 2}\Omega_{3i}^{-1}A_{i2}^{\eta 1}, F_{\eta 3}\Omega_{3i}^{-1}A_{i2}^{\eta 1}, 0\Big)^{\mathrm{T}},$$

$$\mathbf{r}_5 = \Big(0,0,0,F_{\eta 1}\Omega_{1i}^{-1}A_{i3}^{\eta 1}, F_{\eta 2}\Omega_{1i}^{-1}A_{i3}^{\eta 1}, F_{\eta 3}\Omega_{1i}^{-1}A_{i3}^{\eta 1} - 1, F_{\eta 1}\Omega_{1i}^{-1}A_{i3}^{\eta 1}F_{\eta 2}\Omega_{1i}^{-1}A_{i3}^{\eta 1}, F_{\eta 3}\Omega_{1i}^{-1}A_{i3}^{\eta 1}, F_{\eta 1}\Omega_{3i}^{-1}A_{i3}^{\eta 1}, F_{\eta 2}\Omega_{3i}^{-1}A_{i3}^{\eta 1}, F_{\eta 3}\Omega_{3i}^{-1}A_{i3}^{\eta 1}, 0\Big)^{\mathrm{T}},$$

$$\mathbf{r}_6 = \left(0,0,0,F_{\eta1}\Omega_{1i}^{-1}A_{i2}^{\eta2},F_{\eta2}\Omega_{1i}^{-1}A_{i2}^{\eta2},F_{\eta3}\Omega_{1i}^{-1}A_{i2}^{\eta2},F_{\eta1}\Omega_{1i}^{-1}A_{i2}^{\eta2}F_{\eta2}\Omega_{1i}^{-1}A_{i2}^{\eta2}-1,F_{\eta3}\Omega_{1i}^{-1}A_{i2}^{\eta2},F_{\eta1}\Omega_{3i}^{-1}A_{i2}^{\eta2},F_{\eta2}\Omega_{3i}^{-1}A_{i2}^{\eta2},F_{\eta3}\Omega_{3i}^{-1}A_{i2}^{\eta2},0\right)^{\mathrm{T}},$$

$$\mathbf{r}_7 = \left(0,0,0,F_{\eta1}\Omega_{1i}^{-1}A_{i3}^{\eta2},F_{\eta2}\Omega_{1i}^{-1}A_{i3}^{\eta2},F_{\eta3}\Omega_{1i}^{-1}A_{i3}^{\eta2},F_{\eta1}\Omega_{2i}^{-1}A_{i3}^{\eta2}F_{\eta2}\Omega_{2i}^{-1}A_{i3}^{\eta2},F_{\eta3}\Omega_{2i}^{-1}A_{i3}^{\eta2}-1,F_{\eta1}\Omega_{3i}^{-1}A_{i3}^{\eta2},F_{\eta2}\Omega_{3i}^{-1}A_{i3}^{\eta2},F_{\eta3}\Omega_{3i}^{-1}A_{i3}^{\eta2},0\right)^{\mathrm{T}},$$

$$\mathbf{r}_8 = \left(0,0,0,F_{\eta1}\Omega_{1i}^{-1}A_{i2}^{\eta3},F_{\eta2}\Omega_{1i}^{-1}A_{i2}^{\eta3},F_{\eta3}\Omega_{1i}^{-1}A_{i2}^{\eta3},F_{\eta1}\Omega_{2i}^{-1}A_{i2}^{\eta3}F_{\eta2}\Omega_{2i}^{-1}A_{i2}^{\eta3},F_{\eta3}\Omega_{2i}^{-1}A_{i2}^{\eta3},F_{\eta1}\Omega_{3i}^{-1}A_{i2}^{\eta3},F_{\eta2}\Omega_{3i}^{-1}A_{i2}^{\eta3}-1,F_{\eta3}\Omega_{3i}^{-1}A_{i2}^{\eta3},0\right)^{\mathrm{T}},$$

$$\mathbf{r}_9 = \left(0,0,0,F_{\eta1}\Omega_{1i}^{-1}A_{i3}^{\eta3},F_{\eta2}\Omega_{1i}^{-1}A_{i3}^{\eta3},F_{\eta3}\Omega_{1i}^{-1}A_{i3}^{\eta3},F_{\eta1}\Omega_{2i}^{-1}A_{i3}^{\eta3}F_{\eta2}\Omega_{2i}^{-1}A_{i3}^{\eta3},F_{\eta3}\Omega_{2i}^{-1}A_{i3}^{\eta3},F_{\eta1}\Omega_{3i}^{-1}A_{i3}^{\eta3},F_{\eta2}\Omega_{3i}^{-1}A_{i3}^{\eta3},F_{\eta3}\Omega_{3i}^{-1}A_{i3}^{\eta3}-1,0\right)^{\mathrm{T}},$$

$$\mathbf{r}_{10} = \left(0,0,0,-F_{\eta1}\Omega_{1i}^{-1}B_i^{\eta},-F_{\eta2}\Omega_{1i}^{-1}B_i^{\eta},-F_{\eta3}\Omega_{1i}^{-1}B_i^{\eta},-F_{\eta1}\Omega_{2i}^{-1}B_i^{\eta}-F_{\eta2}\Omega_{2i}^{-1}B_i^{\eta},-F_{\eta3}\Omega_{2i}^{-1}B_i^{\eta},-F_{\eta1}\Omega_{3i}^{-1}B_i^{\eta},-F_{\eta2}\Omega_{3i}^{-1}B_i^{\eta},-F_{\eta3}\Omega_{3i}^{-1}B_i^{\eta},1\right)^{\mathrm{T}},$$

$$\mathbf{r}_{11} = \frac{1}{2}\Big((\mathcal{D}\mathbf{Q})_{13}^{-1},(\mathcal{D}\mathbf{Q})_{23}^{-1},(\mathcal{D}\mathbf{Q})_{33}^{-1},-F_{\eta1}(\mathcal{D}^2\mathbf{Q})_{13}^{-1},-F_{\eta2}(\mathcal{D}^2\mathbf{Q})_{13}^{-1},-F_{\eta3}(\mathcal{D}^2\mathbf{Q})_{13}^{-1},-F_{\eta1}(\mathcal{D}^2\mathbf{Q})_{23}^{-1},-F_{\eta2}(\mathcal{D}^2\mathbf{Q})_{23}^{-1},-F_{\eta3}(\mathcal{D}^2\mathbf{Q})_{23}^{-1},$$
$$-F_{\eta1}(\mathcal{D}^2\mathbf{Q})_{33}^{-1},-F_{\eta2}(\mathcal{D}^2\mathbf{Q})_{33}^{-1},-F_{\eta3}(\mathcal{D}^2\mathbf{Q})_{33}^{-1},0\Big)^{\mathrm{T}},$$

$$\mathbf{r}_{12} = \frac{1}{2}\Big((\mathcal{D}\mathbf{Q})_{12}^{-1},(\mathcal{D}\mathbf{Q})_{22}^{-1},(\mathcal{D}\mathbf{Q})_{32}^{-1},-F_{\eta1}(\mathcal{D}^2\mathbf{Q})_{12}^{-1},-F_{\eta2}(\mathcal{D}^2\mathbf{Q})_{12}^{-1},-F_{\eta3}(\mathcal{D}^2\mathbf{Q})_{12}^{-1},-F_{\eta1}(\mathcal{D}^2\mathbf{Q})_{22}^{-1},-F_{\eta2}(\mathcal{D}^2\mathbf{Q})_{22}^{-1},-F_{\eta3}(\mathcal{D}^2\mathbf{Q})_{22}^{-1},$$
$$-F_{\eta1}(\mathcal{D}^2\mathbf{Q})_{32}^{-1},-F_{\eta2}(\mathcal{D}^2\mathbf{Q})_{32}^{-1},-F_{\eta3}(\mathcal{D}^2\mathbf{Q})_{32}^{-1},0\Big)^{\mathrm{T}},$$

$$\mathbf{r}_{13} = \frac{1}{2}\Big((\mathcal{D}\mathbf{Q})_{11}^{-1},(\mathcal{D}\mathbf{Q})_{21}^{-1},(\mathcal{D}\mathbf{Q})_{31}^{-1},-F_{\eta1}(\mathcal{D}^2\mathbf{Q})_{11}^{-1},-F_{\eta2}(\mathcal{D}^2\mathbf{Q})_{11}^{-1},-F_{\eta3}(\mathcal{D}^2\mathbf{Q})_{11}^{-1},-F_{\eta1}(\mathcal{D}^2\mathbf{Q})_{21}^{-1},-F_{\eta2}(\mathcal{D}^2\mathbf{Q})_{21}^{-1},-F_{\eta3}(\mathcal{D}^2\mathbf{Q})_{21}^{-1},$$
$$-F_{\eta1}(\mathcal{D}^2\mathbf{Q})_{31}^{-1},-F_{\eta2}(\mathcal{D}^2\mathbf{Q})_{31}^{-1},-F_{\eta3}(\mathcal{D}^2\mathbf{Q})_{31}^{-1},0\Big)^{\mathrm{T}}.$$

References

[1] D.S. Balsara, C. Shu, Monotonicity preserving weighted essentially non-oscillatory schemes with increasingly high order accuracy, J. Comp. Phys. 160 (2000) 405.
[2] P.T. Barton, D. Drikakis, E. Romenski, V.A. Titarev, Exact and approximate solutions of Riemann problems in non-linear elasticity, J. Comp. Phys. 228 (2009) 7046.
[3] P.T. Barton, D. Drikakis, E. Romenski, An Eulerian finite-volume scheme for large elastoplastic deformations in solids, Int. J. Num. Meth. Eng. 81 (2010) 453.
[4] D. Enright, R. Fedkiw, J. Ferziger, I. Mitchell, A hybrid particle level set method for improved interface capturing, J. Comp. Phys. 183 (2002) 83.
[5] R.P. Fedkiw, T. Aslam, B. Merriman, S. Osher, A non-oscillatory Eulerian approach to interfaces in multimaterial flows (the ghost fluid method), J. Comp. Phys. 152 (1999) 457.
[6] R.P. Fedkiw, Coupling an Eulerian fluid calculation to a Lagrangian solid calculation with the ghost fluid method, J. Comp. Phys. 175 (2002) 200.
[7] S.K. Godunov, E.I. Romenskii, Elements of Continuum Mechanics and Conservation Laws, Kluwer Academic/Plenum Publishers, 2003.
[8] D. Hartmann, M. Meinke, W. Schröder, The constrained reinitialization equation for level set methods, J. Comp. Phys. 229 (2010) 1514.
[9] X.Y. Hu, B.C. Khoo, N.A. Adams, F.L. Huang, A conservative interface method for compressible flows, J. Comp. Phys. 219 (2006) 553.
[10] G.S. Jiang, C.W. Shu, Efficient implementation of weighted ENO schemes, J. Comp. Phys. 126 (1996) 202.
[11] G.S. Jiang, D. Peng, Weighted ENO schemes for Hamilton–Jacobi equations, SIAM J. Sci. Comp. 21 (1999) 2126.
[12] A. Juanicotena, Experimental investigation of dynamic friction at high contact pressure applied to an aluminium/stainless steel tribo pair, J. Phys. IV 134 (2006) 559.
[13] V.I. Kondaurov, Equations of elastoviscoplastic medium with finite deformations, J. App. Mech. Tech. Phys. 23 (1982).
[14] P.G. LeFloch, F. Olsson, A second-order Godunov method for the conservation laws of nonlinear elastodynamics, Impact Comp. Sci. Eng. 2 (1990) 318.
[15] T.G. Liu, B.C. Khoo, K.S. Yeo, Ghost fluid method for strong shock impacting on material interface, J. Comp. Phys. 190 (2003) 651.
[16] T.G. Liu, B.C. Khoo, The accuracy of the modified ghost fluid method for gas–gas Riemann problem, App. Num. Math. 57 (2007) 721.
[17] T.G. Liu, W.F. Xie, B.C. Khoo, The modified ghost fluid method for coupling of fluid and structure constituted with hydro-elasto-plastic equation of state, SIAM J. Sci. Comp. 30 (2008) 1105.
[18] G.H. Miller, P. Colella, A high-order Eulerian Godunov method for elastic-plastic flow in solids, J. Comp. Phys. 167 (2001) 131.
[19] G.H. Miller, P. Colella, A conservative three-dimensional Eulerian method for coupled solid-fluid shock capturing, J. Comp. Phys. 183 (2002) 26.
[20] G.H. Miller, An iterative Riemann solver for systems of hyperbolic conservation laws, with application to hyperelastic solid mechanics, J. Comp. Phys. 193 (2003) 198.
[21] R.R. Nourgaliev, T.G. Theofanous, High-fidelity interface tracking in compressible flows: unlimited anchored adaptive level set, J. Comp. Phys. 224 (2007) 836.
[22] B.J. Plohr, D.H. Sharp, A conservative Eulerian formulation of the equations for elastic flow, Adv. Appl. Math. 9 (1988) 418.
[23] B.J. Plohr, D.H. Sharp, A conservative formulation for plasticity, Adv. Appl. Math. 13 (1992) 462.
[24] W.J. Rider, D.B. Kothe, Stretching and tearing interface tracking methods, AIAA-95-1717-CP, 1995.
[25] E.I. Romensky, Thermodynamics and hyperbolic systems of balance laws in continuum mechanics, in: E.F. Toro (Ed.), Godunov Methods: Theory and Applications, Kluwer Academic/Plenum Publishers, 2001.
[26] C. Shu, S. Osher, Efficient implementation of essentially non-oscillatory shock-capturing schemes, J. Comp. Phys. 77 (1988) 439.
[27] M. Sussman, P. Smereka, S. Osher, A level set approach for computing solutions to incompressible two-phase flow, J. Comp. Phys. 114 (1994) 146.
[28] V.A. Titarev, E. Romenski, E.F. Toro, MUSTA-type upwind fluxes for non-linear elasticity, Int. J. Numer. Meth. Eng. 73 (2008) 897.

[29] L.B. Tran, H.S. Udaykumar, A particle-level set-based sharp interface cartesian grid method for impact, penetration, and void collapse, J. Comp. Phys. 193 (2004) 469.
[30] J. Walter, D. Yu, B.J. Plohr, J. Grove, J. Glimm, An algorithm for Eulerian front tracking for solid deformation, Stony Brook AMS Preprint; SUNYSB-AMS-00-24, 2000.
[31] F. Wang, J.G. Glimm, J.W. Grove, B.J. Plohr, A conservative Eulerian numerical scheme for elastoplasticity and application to plate impact problems, Impact Comp. Sci. Eng. 5 (1993) 285.
[32] R.E. Winter, G.J. Ball, P.T. Keightley, Mechanisms of shock-induced dynamic friction, J. Phys. D 39 (2006) 5043.
[33] P. Woodward, P. Colella, The numerical simulation of two-dimensional fluid flow with strong shocks, J. Comp. Phys. 54 (1984) 115.
[34] W.F. Xie, Y.L. Young, T.G. Liu, Multiphase modeling of dynamic fluid-structure interaction during close-in explosion, Int. J. Numer. Meth. Eng. 74 (2008) 1019.